

Ru-Sn oxide/C supported Pt anode catalysts for direct ethanol fuel cells

by

©Binyu Chen

A thesis submitted to the School of Graduate Studies in partial fulfillment of the requirements for the degree of

Master of Science

Department of Chemistry

Memorial University of Newfoundland

August 2018

St. John's

Newfoundland

Abstract

Direct alcohol fuel cells are promising power sources. Ethanol has recently attracted much attention since it is renewable, relatively safe and has a high energy density. In order to make best use of ethanol in fuel cells, many Pt-based catalysts have been studied. However, the low electrochemical activity of ethanol at the low potentials required for fuel cells has limited the development of direct ethanol fuel cells. This thesis describes the use of carbon black modified with Ru-Sn mixed oxides as supports for Pt nanoparticles. Since the Pt nanoparticles are on the surface of the Ru-Sn oxide, the promoting effect of Ru-Sn oxide is achieved, while the blockage of Pt active sites is minimized. Therefore, the high carbon dioxide selectivity of Pt can be retained and the performance at low potentials can be improved. The effects of reaction conditions, including Ru:Sn:C ratios, Pt loading, and heat treatment, have been investigated. Cyclic voltammetry allows rapid determination of the electrochemical performance of catalysts for preliminary screening. Product distribution results from an ethanol electrolysis cell provide the faradaic efficiency and mechanistic information. The best Pt-RuSnO₂/C catalyst showed better catalytic activity towards ethanol oxidation at low potentials than that of commercial Pt/C catalyst and retained relatively high faradaic efficiency.

Acknowledgements

I would first like to thank my supervisor Dr. Peter Pickup for his continuous support throughout my M.Sc. study. His door was always open whenever I ran into problems or had questions. His patient guidance and profound knowledge have made my research enjoyable and unforgettable. I could not have imagined having a better supervisor.

I would also like to thank my supervisory committee members: Dr. Christopher Kozak and Dr. Yuming Zhao, for their advice, comments and encouragement. I thank all the faculty members who have taught me courses and broadened my knowledge. I acknowledge the support staff who trained me on the various instruments and conducted analyse for my samples.

I would like to express my sincere gratitude to the funding sources who made my program possible: Memorial University and the Natural Science and Engineering Research Council of Canada.

I thank Dr. Pickup's group for their input and support throughout my research. Also I thank my friends for their encouragement throughout the hard times and for the fun we have had in the last two years.

Last but not the least, I would like to express the deepest appreciation to my parents for their unfailing support and continuous encouragement.

Table of Contents

Abstract	ii
Acknowledgments	iii
Table of Contents	vii
List of Tables	viii
List of Figures	xii
List of Abbreviations and Symbols	xii
1 Introduction	1
1.1 Fuel cells	1
1.2 Scientific study of ethanol oxidation	3
1.3 Catalysts for ethanol oxidation	5
1.3.1 Binary catalysts	7
1.3.2 Ternary catalysts	8
1.3.3 Catalysts used in alkaline media	10
1.4 Catalyst supports	10
1.4.1 Carbon materials	10
1.4.2 Non-carbon materials	12

1.5	Pt–metal oxide composite catalysts	13
1.5.1	Titanium oxide	14
1.5.2	Tungsten oxide	15
1.5.3	Molybdenum oxide	17
1.5.4	Tin oxide	17
1.5.5	Ruthenium oxide	19
1.6	Objectives of this thesis	19
2	Experimental	20
2.1	Preparation of Catalysts	20
2.1.1	Chemicals	20
2.1.2	Modifying Carbon Black	21
2.1.3	Pt Deposition	22
2.1.4	Heat Treatment	22
2.2	Preparation of Electrodes and MEAs	22
2.3	Electrochemical Measurements	23
2.4	Product Distribution Measurements	25
2.4.1	Non-Dispersive Infrared (NDIR) Carbon Dioxide Detector	25
2.4.2	Nuclear Magnetic Resonance (NMR) Spectroscopy	25
2.5	Catalyst Characterization	26
2.5.1	Thermogravimetric Analysis (TGA)	26
2.5.2	X-Ray Diffraction (XRD)	26
2.5.3	Inductively Coupled Plasma Optical Emission Spectroscopy (ICP-OES)	27
2.5.4	Scanning Electron Microscopy (SEM) with Energy Dispersive X-Ray Analysis (EDX)	27
2.5.5	Transmission Electron Microscopy (TEM)	28

3	Characterization of the Supports and Catalysts	29
3.1	TGA	29
3.2	XRD	32
3.3	ICP-OES	37
3.4	SEM-EDX	38
3.5	TEM	43
3.6	Conclusions	46
4	Cyclic Voltammetric Analysis	47
4.1	Estimation of Electrochemically Active Surface Area	47
4.2	CV of Ethanol at 30%Pt-RuSnO ₂ /C _{low} (110)	49
4.3	Effect of Various Preparation Conditions	51
4.4	Effect of Heat Treatment and Pt Loading	53
4.5	Conclusions	56
5	Ethanol Electrolysis Cell Results	57
5.1	Introduction	57
5.2	Screening of Catalysts in a 9-Anode Cell	59
5.3	5 cm ² Single-Anode Cell	60
5.4	Conclusions	66
6	Summary and Future Work	67
6.1	Summary	67
6.2	Future Work	68
A	SEM-EDX	70
B	Cyclic voltammograms	72

C EDX spectra from TEM experiments and TEM image	75
Bibliography	76

List of Tables

2.1	RuSnO ₂ /C preparation conditions	21
3.1	TGA results: the effect of reaction time, conditions and carbon content.	31
3.2	Catalyst composition.	38
3.3	SEM-EDX analysis results.	42
5.1	Current and faradic yield of CO ₂ for ethanol oxidation (0.100 M at 0.2 mL min ⁻¹) at different anodes in a 5 cm ² PEM electrolysis cell at 80 °C.	62
5.2	Peak assignment for Figure 5.3 with corresponding components and concentrations.	65
5.3	Currents, chemical yields of products, stoichiometries, and faradaic efficiencies for ethanol oxidation (0.1 M at 0.2 mL min ⁻¹) at 70%Pt/C, 30%Pt/S _{LC} , and 75%PtRu/C anodes in a 5 cm ² PEM electrolysis cell at 80 °C.	65

List of Figures

1.1	A simplified mechanism for ethanol electro-oxidation	4
1.2	Schematic diagram of a product collection system for HPLC analysis.	5
1.3	Schematic diagram of a product collection system for NMR analysis. .	6
1.4	Linear sweep voltammograms (1 mV/s) for electro-oxidation of 1 M ethanol in 0.1 M HClO ₄ (aq) on (a) Pt/C and PtX/C (X = Sn, Ni, Co, Rh, Pd) catalysts, (b) PtSn/C and PtSnM/C (M = Ni, Co, Rh, Pd) catalysts.	9
1.5	Schematic illustration of two possible mechanisms for ethanol oxidation at a metal on a transition metal oxide.	14
1.6	A. Cyclic voltammograms (10 mV/s) of (a) PtRh/C, (b) MoO ₃ -modified PtRh/C and (c)WO ₃ -modified PtRh/C catalysts in 0.5 M H ₂ SO ₄ (aq) containing 0.5 M ethanol. B. Linear sweep voltammograms (10 mV/s) of (a) PtRh/C, (b) MoO ₃ -modified PtRh/C and (c)WO ₃ -modified PtRh/C catalysts in 0.5 M H ₂ SO ₄ (aq) containing 0.5 M ethanol.	16
1.7	Potentiodynamic polarization curves of ethanol electro-oxidation in 0.5 M H ₂ SO ₄ (aq) containing 1 M ethanol on different catalysts. Scan rate 50 mV/s, temperature 20 °C.	18
2.1	Schematic diagram of the nine-anode PEM cell (top) and crossover mode of operation (bottom). R = CH ₃	24

3.1	TGA analysis of (a) as-prepared RuSnO ₂ /C (110), N ₂ gas was switched to air at 600 °C, and (b) RuSnO ₂ /C (110) heated at 200 °C for 20 h, air was used all the time.	30
3.2	XRD patterns of (a) as-prepared RuSnO ₂ /C (110), and (b) RuSnO ₂ /C (110) heated at 200 °C for 20 h.	33
3.3	XRD patterns of (a) 25%Pt-RuSnO ₂ /C (000), (b) 25%Pt-RuSnO ₂ /C (0.057), and (c) 25%Pt-RuSnO ₂ /C (222).	35
3.4	XRD patterns for (a) 70%Pt-RuSnO ₂ /C (110), (b) 25%Pt-RuSnO ₂ /C (110)*, and (c) 25%Pt-RuSnO ₂ /C (110).	36
3.5	SEM images and EDX spectra of 25%Pt-RuSnO ₂ /C (110) (a, c and d) and 70%Pt-RuSnO ₂ /C (110) (b and e).	40
3.6	SEM image of 30%Pt-RuSnO ₂ /C _{low} (110).	41
3.7	TEM of 30%Pt-RuSnO ₂ /C _{low} (110).	44
3.8	TEM image (a), HAADF image (b), line scan analysis (c and d) of 30%Pt-RuSnO ₂ /C _{low} (110).	45
4.1	Cyclic voltammograms (100 mV/s) of (a) 70%Pt/C (Hispec) and (b) 30%Pt-RuSnO ₂ /C _{low} (110) and RuSnO ₂ /C _{low} (110) in 1 M H ₂ SO ₄ (aq).	48
4.2	Cyclic voltammogram (10 mV/s) of 30%Pt-RuSnO ₂ /C _{low} (110) in 1 M H ₂ SO ₄ (aq) containing 0.1 M ethanol.	50
4.3	Cyclic voltammograms (10 mV/s) of 25%Pt-RuSnO ₂ /C catalyst in 1 M H ₂ SO ₄ (aq) containing 0.1 M ethanol. (a) First forward scan and (b) second forward scan.	52
4.4	Cyclic voltammograms (10 mV/s) of different catalysts in 1 M H ₂ SO ₄ (aq) containing 0.1 M ethanol. (a) First forward scan and (b) second forward scan.	54

4.5	Pt utilization: Cyclic voltammograms (10 mV/s) of different catalysts in 1 M H ₂ SO ₄ (aq) containing 0.1 M ethanol. (a) First forward scan and (b) second forward scan.	55
5.1	Comparison of polarization curves for different anode catalysts (4.0 mg Pt cm ⁻²), at 80 °C (except the one labelled 50 °C), in a 9-anode ethanol electrolysis cell operated in a crossover mode (1 M ethanol was passed through the cathode flow field). Representative error bars (standard deviations for 3 electrodes) were shown for two data sets.	59
5.2	Polarization curves for 30%Pt-RuSnO ₂ /C _{low} (110) (2.6 mg Pt cm ⁻²) and 70%Pt/C (Hispec) (3.2 mg Pt cm ⁻²) anode catalysts in a 5 cm ² single-anode cell, at 80 °C, with 0.1 M ethanol (anode) at 0.5 mL min ⁻¹ and N ₂ (cathode) at 34 mL min ⁻¹ . The cathode catalyst was Pt black (4 mg cm ⁻²).	61
5.3	¹ H-NMR (300 MHz) spectrum of a mixture of fumaric acid solution (D ₂ O) and the exhaust solution from EEC operated with 0.1 M ethanol at 0.45 V and 80 °C. Anode catalyst: 30%Pt-RuSnO ₂ /C _{low} (110). . .	64
A.1	SEM image (a) and EDX spectra (b and c) for the ICP-OES digestion residue of 30%Pt-RuSnO ₂ /C _{low} (110)	71
B.1	Cyclic voltammograms (100 mV/s) of 30%Pt-RuSnO ₂ /C (110–200°C) in 1 M H ₂ SO ₄ (aq).	73
B.2	Cyclic voltammograms (100 mV/s) of 30%Pt-RuSnO ₂ /C (110) in 1 M H ₂ SO ₄ (aq).	74
C.1	EDX spectrum of the circled area in Figure 3.7(a).	75
C.2	EDX spectrum of the circled area in Figure 3.7(b).	76

C.3	EDX spectrum of the circled area in Figure 3.7(c).	77
C.4	EDX spectrum of the circled area in Figure 3.7(d).	78
C.5	TEM of 30%Pt-RuSnO ₂ /C _{low} (110) used for particle size calculation.	79

List of Abbreviations and Symbols

AFC	alkaline fuel cell
PEMFC	polymer electrolyte membrane fuel cell
PAFC	phosphoric acid fuel cell
SOFC	solid oxide fuel cell
MCFC	molten carbonate fuel cell
NASA	National Aeronautic and Space Administration
GE	General Electric
PFSA	perfluorinated sulfonic acid
DMFC	direct methanol fuel cell
DEFC	direct ethanol fuel cell
ORR	oxygen reduction reaction
EOR	ethanol oxidation reaction
CV	cyclic voltammetry
ECSA	electrochemically active surface area
AAL	acetaldehyde
AA	acetic acid
FTIR	Fourier transform infrared spectroscopy
DEMS	differential electrochemical mass spectrometry

HPLC	high performance liquid chromatography
NMR	nuclear magnetic resonance
IR	infrared
2,4-DNPH	2,4-dinitrophenylhydrazine
NDIR	non-dispersive infrared
MOR	methanol oxidation reaction
CB	carbon black
CNT	carbon nanotube
CNF	carbon nanofiber
SWCNT	single-walled carbon nanotube
MWCNT	multi-walled carbon nanotube
CVD	chemical vapor deposition
RuSnO ₂ /C	Ru-Sn oxide modified C
EEC	ethanol electrolysis cell
Pt–RuSnO ₂ /C	RuSnO ₂ /C supported Pt nanoparticle
MEA	membrane electrode assembly
CFP	carbon fiber paper
GC	glassy carbon
SCE	saturated calomel reference electrode
EtOH	ethanol
TGA	thermogravimetric analysis
XRD	X-ray diffraction
ICP-OES	inductively coupled plasma optical emission spectroscopy
PFA	perfluoroalkoxy alkane
SEM	scanning electron microscopy

EDX energy dispersive X-ray analysis
TEM transmission electron microscopy
FC fuel cell
PEM proton exchange membrane

Chapter 1

Introduction

1.1 Fuel cells

The fuel cell was invented by William Grove in 1839 [1]. It can directly convert chemical energy into electric energy with a high efficiency. Depending on the electrolyte, fuel cells can be divided into alkaline fuel cells (AFCs), polymer electrolyte membrane fuel cells (PEMFCs), phosphoric acid fuel cells (PAFCs), solid oxide fuel cells (SOFCs) and molten carbonate fuel cells (MCFCs).

AFCs, using aqueous alkali as the electrolyte, are one of the oldest types of fuel cell technologies. They have been applied to Apollo series missions and space shuttles by the National Aeronautic and Space Administration (NASA) since the 1960s [2]. However, because CO_2 will react with the liquid electrolyte to lower the performance of AFCs, a high purity of fuel gases is required, which limits the applications of AFCs [1, 2].

The first generation PEMFCs, manufactured by General Electric (GE), were applied to the Gemini space missions. Polystyrene sulfonic acid membranes were initially used in these PEMFCs [2]. However, these PEMFCs, mainly restricted by the

membrane's poor conductivity and stability, showed poor performance and limited lifetimes. In the mid-1960s, a perfluorinated sulfonic acid (PFSA) membrane, known as Nafion, manufactured by DuPont showed great potential for PEMFCs because of its excellent physical properties and oxidation stability [3].

PAFCs, using liquid phosphoric acid as the electrolyte, are normally operated at ca. 200 °C [1]. While PAFCs can tolerate up to 2% CO and be operated with less purified fuel gas than AFCs, applications are limited by their relatively high cost because they need Pt-based catalysts to speed up the reactions and also require highly corrosion resistant materials against phosphoric acid [1, 2].

Molten carbonates serve as the electrolyte in MCFCs and solid oxides or ceramic materials work as the electrolyte in SOFCs. Both MCFCs and SOFCs can be operated without the presence of precious metal catalysts (such as Pt) at high temperatures. They have higher cell efficiencies than PAFCs [2] and the use of waste heat to generate more electricity (cogeneration) can further increase overall efficiencies.

Fuel cells can also be classified according to their fuel types. Hydrogen fuel cells are the most developed ones. However, hydrogen is explosive and highly flammable, and its storage normally requires a very high pressure. For small-size and mid-size applications, such as portable devices and vehicles, simplicity of the fuel cell is necessary. Hence, the use of PEMFCs is normally the first option. If using hydrogen as the fuel, humidification of hydrogen is required to keep the solid electrolyte membrane hydrated, which makes the design of fuel cells complicated. As a result of these concerns (safety, storage, and simplicity), liquid fuels, such as methanol, ethanol and formic acid, have aroused wide interest. Direct methanol fuel cells (DMFCs) were developed before direct ethanol fuel cells (DEFCs), which are still not close to commercialization. The use of ethanol is preferable to the use of methanol because of its lower toxicity, better sustainability, and higher energy density [4, 5].

DEFCs can be operated under both acidic and basic conditions. Although the oxygen reduction reaction (ORR) in the presence of a base has faster kinetics than that of an acid, the development of alkaline DEFCs has been restricted by problems such as the formation of carbonate, and low conductivities of anion exchange membranes [4]. As for acidic DEFCs, one of the main issues is the slow kinetics of the ethanol oxidation reaction (EOR), which requires better anode catalysts to increase their electrochemical activity. Therefore, the development of anode catalysts for acidic DEFCs is very important. All experiments in this work are related to DEFCs with acidic membranes.

1.2 Scientific study of ethanol oxidation

To develop novel efficient electrocatalysts for DEFCs, it is necessary to understand the mechanism of EOR. Cyclic voltammetry (CV) is a routine method for investigating EOR because it is simple, quick, and can provide valuable kinetic and thermodynamic information. CO stripping voltammetry can not only be applied for the study of morphology and structure, but also provide an accurate estimation of electrochemically active surface area (ECSA) [6]. However, voltammetry can not provide product information which is crucial for mechanistic investigations.

It is commonly accepted that acetaldehyde (AAL), acetic acid (AA) and CO_2 are the main products in EOR [7–9]. A simplified mechanism is shown in Figure 1.1 where some steps such as adsorption of OH from water and generation of protons have not been included. The corresponding number of electrons (per ethanol molecule) for different pathways are indicated.

To obtain information on intermediates and products, many different analytical techniques have been applied, such as Fourier transform infrared spectroscopy (FTIR) [7, 9–11], differential electrochemical mass spectrometry (DEMS) [6, 9, 11],

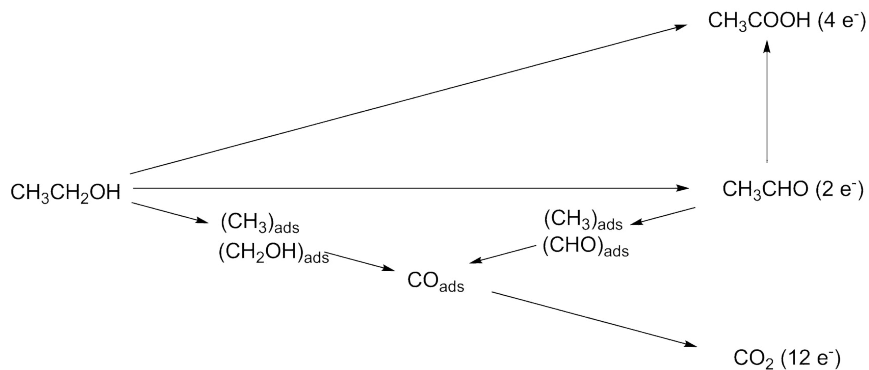


Figure 1.1: A simplified mechanism for ethanol electro-oxidation [7, 8].

high performance liquid chromatography (HPLC) [12] and nuclear magnetic resonance (NMR) spectroscopy [13].

FTIR can be used to obtain an infrared (IR) spectrum of a solid, liquid, or gas. When an organic molecule is irradiated with infrared light, the vibrational modes of chemical bonds or functional groups in the molecule can absorb IR radiation. Different chemical bonds or functional groups have different absorption frequencies, which will occur at different positions in the IR spectrum. Therefore, it is a useful technique for the study of EOR. For example, Vigier et al. [10] used FTIR to identify the adsorbed intermediates and reaction products on some catalyst's surface. This allowed them to propose a mechanism for EOR on Pt and PtSn catalysts.

DEMS is another analytical technique which can be used to investigate the mechanism of EOR. It combines an electrochemical half-cell with a mass spectrometer and measures gaseous and volatile products in real time. Compared to the IR technique, DEMS has a lower detection limit and can provide more reliable quantitative information.

HPLC and NMR are also useful techniques for the investigation of ethanol oxidation since both of them can be used to identify and quantify the products of EOR. Combined with various detectors, such as UV detectors and mass spectrometry,

ters, HPLC can provide quantitative and qualitative information. Rousseau et al. [12] used 2,4-dinitrophenylhydrazine (2,4-DNPH) to trap AAL, and sodium hydroxide solution to trap CO_2 (as shown in Figure 1.2). Two different columns were used according to the analytes. A UV detector and a refractometer detector were used in their experiments.

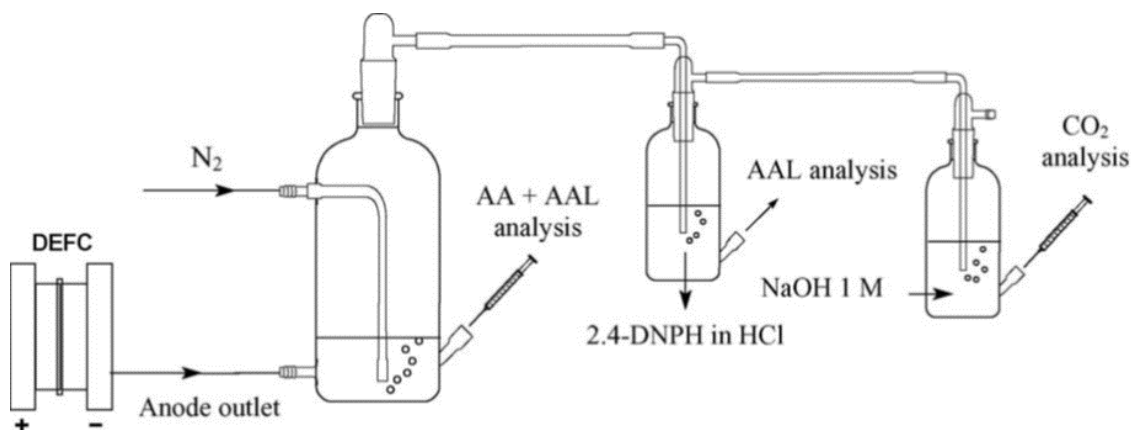


Figure 1.2: Schematic diagram of a product collection system for HPLC analysis. Reprinted from ref. [12]. Copyright 2006, with permission from Elsevier.

Altarawneh *et al.* [13] combined NMR with a non-dispersive infrared (NDIR) CO_2 detector to get product distributions (shown in Figure 1.3). With the help of an internal standard, the concentration of AA, AAL and ethanol were determined from NMR. The CO_2 concentration was measured by a CO_2 detector.

1.3 Catalysts for ethanol oxidation

Ethanol can be oxidized in both acidic and alkaline media. In both media, it requires highly electro-active catalysts to improve the sluggish oxidation kinetics. In acidic media, the only stable and active catalyst for EOR is Pt, which is able to adsorb ethanol and break the C-H bonds [14]. But Pt is easily poisoned by the strongly adsorbed CO intermediate formed during EOR, which decreases the number of active

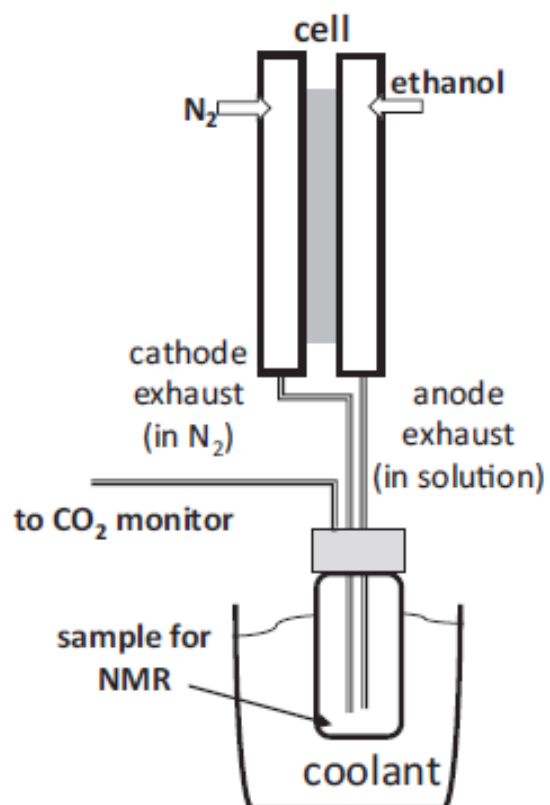


Figure 1.3: Schematic diagram of a product collection system for NMR analysis. Reprinted from ref. [13].

sites. To remove the strongly adsorbed CO, a high over-potential is required. However, for practical DEFCs, the potential of the anode should be low enough to allow the cell to operate with a reasonable efficiency. Moreover, it is necessary to have a low Pt loading without performance compromise since Pt is precious and very expensive. Generally, there are two strategies to design catalysts for DEFCs. One is alloying Pt with other non-precious metals, such as Ru, Sn, W, and Mo, to decrease CO poisoning at low potentials. Another one is a support strategy. A suitable high surface area support can help Pt distribute evenly with a narrow nanoscale size, which can maximize the utilization of Pt and reduce the Pt loading. In Section 1.3, Pt alloyed with various non-precious metals for acidic DEFCs is mainly discussed and catalysts for alkaline DEFCs will be briefly reviewed. Different types of catalyst supports are introduced in Section 1.4.

1.3.1 Binary catalysts

Since the proton exchange membrane creates a low pH condition in a DEFC, the second metal added to modify Pt should not only be able to reduce CO poisoning at low potentials, but also have good stability in acidic media. Therefore, there are not too many choices of the second metal species [14].

PtRu/C (PtRu alloy supported by carbon) catalysts provide high activity and stability for the methanol oxidation reaction (MOR) and are also widely used in DEFC development. It is well known that the catalytic activities of PtRu/C catalysts are strongly dependent on the preparation method [15]. Liu et al. [16] reviewed three important methods (the impregnation method, the colloidal method and the microemulsion method) for preparing carbon supported PtRu catalysts. Great progress has been made to improve these methods [17].

Sn is known to activate water at low potentials, which can provide OH species to

remove adsorbed CO from Pt surface [14,18]. PtSn/C is the best binary catalyst for ethanol electro-oxidation in acidic media [4,18]. While preparing PtSn/C catalysts, it is difficult to maintain Sn in a metallic state [14]. The enhanced catalytic activity seems to be due to both non-alloyed Sn and alloyed Sn [18]. Friedl and Stimming [19] concluded that both of alloyed Sn and Sn oxide are important for the reaction mechanism. Beyhan et al. [20] compared a PtSn/C catalyst with some other binary catalysts (Ni, Co, Rh, and Pd). As shown in Figure 1.4(a), at 500 mV vs. RHE, PtSn/C gave the highest catalytic activity while other binary catalysts showed quite similar catalytic activities.

1.3.2 Ternary catalysts

While PtSn/C catalysts exhibit higher catalytic activity towards ethanol oxidation, they produce more AA and AAL, but less CO₂ compared to Pt/C catalysts. As shown in Figure 1.1, producing CO₂ will give three times more electrons than producing AA. Hence, it is necessary to design a novel catalyst which is highly active at low potentials and produces high yields of CO₂. Adding a third metal has been considered, although the preparation of ternary catalysts is more difficult.

As shown in Figure 1.4(b), both PtSnNi/C and PtSnCo/C showed superior catalytic activity in low potential regions. These ternary catalysts were also examined in a DEFC. The maximum power density (at 80 °C) of PtSnCo/C was about 34 mW cm⁻² and it is almost 6 times higher than that of Pt/C and 3 times higher than that of PtSn/C. However, the PtSnCo/C catalyst showed poor durability when it was tested by a chronoamperometric method. It is also worthy to note that Beyhan et al. [20] did not report product distributions. So the influence of adding a third metal towards the CO₂ yield is unknown.

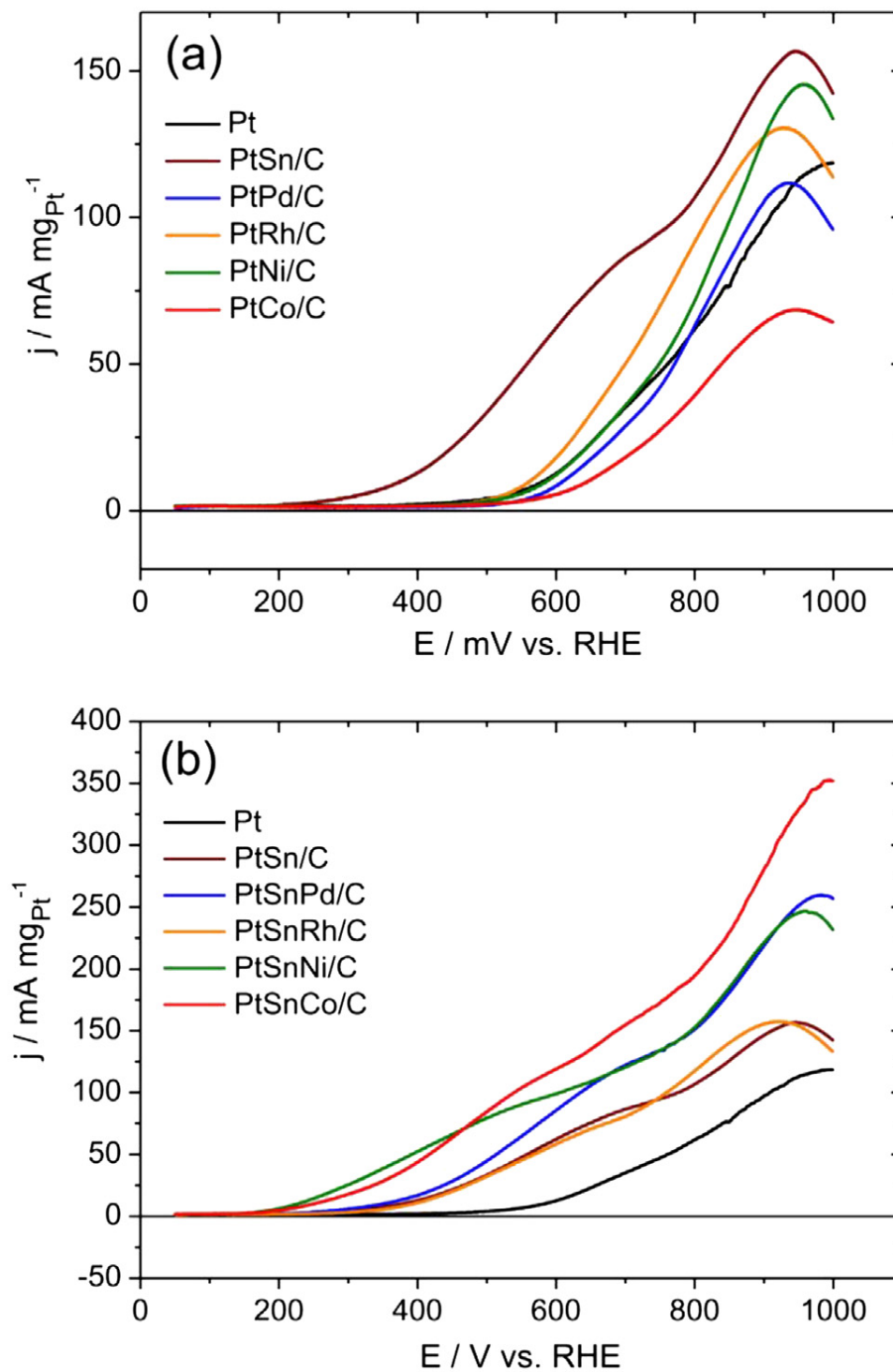


Figure 1.4: Linear sweep voltammograms (1 mV/s) for electro-oxidation of 1 M ethanol in 0.1 M $\text{HClO}_4(\text{aq})$ on (a) Pt/C and PtX/C (X = Sn, Ni, Co, Rh, Pd) catalysts, (b) PtSn/C and PtSnM/C (M = Ni, Co, Rh, Pd) catalysts. Reprinted from ref. [20]. Copyright 2013, with permission from Elsevier.

1.3.3 Catalysts used in alkaline media

Among pure metals, Pd is the most active catalyst for EOR in alkaline media [21]. Similar to Pt, Pd also has a CO poisoning problem which limits its performance in alkaline DEFCs. Hence, different metals and metal oxides have been considered to improve the catalytic activity of Pd. Unlike in acidic media, a wide variety of metals can be combined with Pd in alkaline media to improve its poison tolerance and promote EOR. For example, Ni is a very popular choice for pairing with Pd and it is much cheaper than Ru. Metal oxides such as CeO_2 , Co_3O_4 , Mn_3O_4 and NiO have also been considered as co-catalysts for Pd [18]. In addition to these Pd-based catalysts, some other catalysts such as Au, tungsten carbide (WC), and Ir, have been reported [4].

1.4 Catalyst supports

An ideal catalyst support for fuel cells should have properties such as (i) high surface area and good catalyst-support interaction for high catalyst dispersion, (ii) suitable porosity for good mass transport (reactants, products, and by-products), (iii) good electrical conductivity for rapid electron transfer, and (iv) high chemical stability [21, 22].

1.4.1 Carbon materials

Carbon materials are widely used as fuel cell catalyst supports. Compared with ceramic oxides, such as alumina and MgO , carbon materials can provide higher surface area, have higher conductivity, and have better stability under both highly acidic and basic conditions [21, 23]. Carbon blacks (CBs) are one of the most studied carbon materials. Non-conventional carbon materials, such as mesoporous carbons, carbon

nanotubes (CNTs), carbon nanofibers (CNFs), and graphene, have drawn more attention recently because of their excellent electrical and mechanical properties.

CBs are prepared by the incomplete combustion or thermal decomposition of hydrocarbons and consist of primary near-spherical particles (< 50 nm) which are aggregated by crystalline domains (< 2 nm). The further aggregation and agglomeration of these primary particles results in a porous high surface area system [22, 23]. Depending on the preparation conditions and source materials, CBs can be commonly subdivided into thermal black, acetylene black, channel black, furnace black and lamp black, and their surface properties are quite variable. For example, Black Pearls 2000 (a furnace black from Cabot Corp.) has a surface area of $1500 \text{ m}^2/\text{g}$, while the surface area of Denka black (an acetylene black from Denka) is only $65 \text{ m}^2/\text{g}$ [24].

Although CBs are important catalyst supports for fuel cells, they have drawbacks such as low thermal and electrical stability, and high micro-porosity [1, 22]. To better control carbon composition, (e.g. pore size, pore distribution, surface area, surface functionality, and graphitization degree), the synthesis of mesoporous carbons with tailored properties has been reported [1, 25]. The preparation methods of these types of carbons can be mainly divided to the sol-gel method, the hard template method, and the soft template method, depending on the precursors and procedures used [1].

CNTs were first reported by Iijima in 1991 [23]. They have a tubular shape composed of a single or multiple wrapped graphene layers of hexagonally arranged carbon atoms and can be simply categorized as single-walled carbon nanotubes (SWCNTs) and multi-walled carbon nanotubes (MWCNTs). The diameter of CNTs is only a few nanometers (2-50 nm) while the length can be up to several millimeters [1]. Due to the entire sp^2 hybridization of carbon atoms, CNTs often exhibit high tensile modulus and high strength [1, 22].

CNFs are a type of carbon fibers whose diameters are less than 500 nm. Unlike

CNTs whose graphene layers are continuously wrapped and parallel to the fibril axis, the graphene layers of CNFs can be vertical, inclined, or even coiled with respect to the fibril axis. These different forms of CNFs can be produced by using various methods, conditions, catalysts, and carbon sources [26]. Chemical vapor deposition (CVD) and spinning of the carbon precursor are two main methods to synthesize CNFs. CNFs have shown great potential as catalyst supports in fuel cells due to their high electrical and thermal conductivity, superior chemical stability and unique one dimensional structure [27]. Both primary CNTs and CNFs are chemically inert and so modification is required to provide anchoring sites for catalyst nanoparticles and enhance the interaction between the carbon surface and catalyst nanoparticles [22,28].

Graphene is a two-dimensional material and consists of a monolayer of carbon atoms with hexagonal lattices. Due to its unique structure, large surface area (theoretically, 2630 m²/g) and high conductivity [22,29], graphene is a promising material as a catalyst support. Graphene sheets can be obtained by various methods such as epitaxial growth of graphene on metal surfaces using chemical vapor deposition, epitaxial growth of graphene on silicon carbide (SiC) through ultra-high vacuum annealing of SiC surface, and reduction of graphene oxide which can be separated by a chemical or thermal exfoliation of graphite oxide sheets. Reduction of graphene oxide is one of the most used methods due to its relatively low cost, high availability and easy modification [30].

1.4.2 Non-carbon materials

Although carbon supports have been widely used for commercial Pt catalysts, the durability of carbon supported catalysts remains a problem. Metal oxides, such as titanium oxide, tin oxide and tungsten oxide, have been extensively investigated as fuel cell catalyst supports due to their high corrosion resistance and co-catalytic effects

[31].

In addition to carbons and metal oxides, the use of conducting polymers as supports has also been widely reported [32]. However, as fuel cell supports, they (carbons, metal oxides and polymers) all have some limitations. For example, carbons are normally not durable in the cathode, metal oxides have relatively low surface area, and polymers have relatively low electrical conductivity. Therefore, combining them together to make hybrid supports has also attracted much interests.

1.5 Pt–metal oxide composite catalysts

As discussed in Section 1.3, the preparation of bi-metallic Pt-M (M=Ru, Sn, Ni, and so on) alloys can be difficult and tri-metallic alloys are even more difficult to prepare. Since the late 1990s, the use of metal oxides as supports and/or as co-catalysts has drawn much attention. Many studies have proved that metal oxides can enhance the catalytic activity of Pt nanoparticles in acidic media. Figure 1.5 shows two possible mechanisms for enhancement of EOR on metal oxide supported Pt. One is the bifunctional mechanism in which the OH groups on the oxide surface assist the removal of CO from the surface of catalytic metals (e.g., Pt). The other one is an electronic mechanism in which the metal-oxide interactions may change the electronic structure of the catalytic metal and promote the charge transfer [33].

The common requirements for metal oxide materials are (i) high chemical stability, (ii) high corrosion resistance under the fuel cell operating conditions, (iii) good electronic conductivity, (iv) some proton conductivity and (v) strong interactions with catalytic metal nanoparticles [34,35]. In this Section, several important metal oxides are discussed.

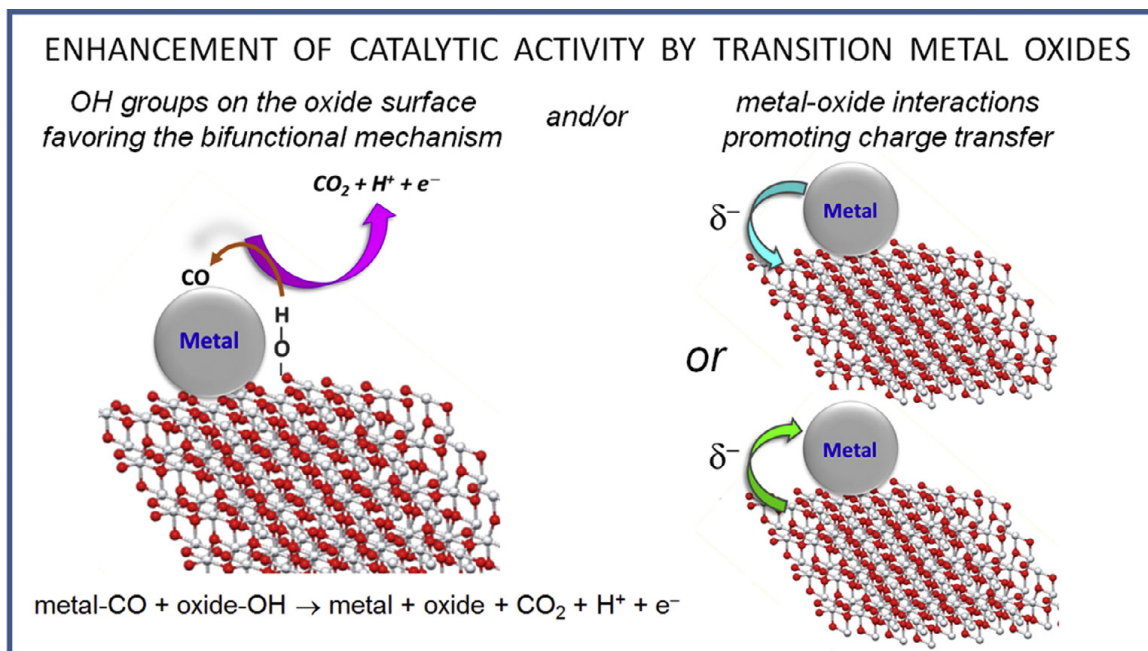


Figure 1.5: Schematic illustration of two possible mechanisms for ethanol oxidation at a metal on a transition metal oxide. Reprinted from ref. [33]. Copyright 2017, with permission from Elsevier.

1.5.1 Titanium oxide

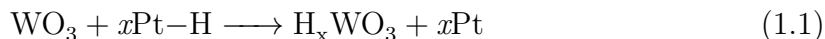
Titanium typically forms stoichiometric titanium dioxide (TiO_2), which is a semiconductor. In addition, titanium oxides can exist in other sub-stoichiometric forms (e.g., Ti_4O_7). Because of their high chemical and electrochemical stability, easy availability, non-toxicity, and relatively low cost, titanium oxides have been widely studied as supports and co-catalysts in fuel cells. It is well known that TiO_2 can help metal nanoparticles disperse well and avoid agglomeration, due to strong metal-oxide interactions. But the electrical conductivity of TiO_2 at 298 K is only $10^{-13} \Omega^{-1} \text{ cm}^{-1}$ [31]. Hence, many methods, such as partially reduction of TiO_2 , introduction of dopants and mixing with carbons [22, 34, 35], have been employed to increase the electrical conductivity.

Song et al. [36] reported that the addition of TiO_2 nanotubes to a Pt/C catalyst

greatly enhanced its catalytic activity and stability for CO oxidation. Two types of TiO₂ showed different enhancement abilities with TiO₂ nanatubes shifting the CO oxidation potential to a lower potential than TiO₂ prepared by a sol-gel method. He and Hu [37] directly prepared TiO₂ nanorod arrays on a Ti foil by a facile hydrothermal method and then deposited Pt nanoparticles onto TiO₂ nanorod arrays. This Pt/TiO₂/Ti catalyst showed better catalytic activity and higher catalytic stability for EOR compared with Pt/C and Pt/Ti catalysts. It is worth noting that titanium oxide has been less studied for EOR than MOR and ORR.

1.5.2 Tungsten oxide

Tungsten has many oxidation states ranging from -1 to +6 [22]. WO₃, as the stoichiometric form of tungsten(VI) oxide, is an n-type semiconductor. Although WO₃ has low electrical conductivity, as shown in Equations 1.1 and 1.2, it can react with the active hydrogen adsorbed on Pt to form a conductive hydrogen tungsten bronze (H_xWO₃) [34]. Tungsten oxides tends to form tungsten trioxide hydrates which can facilitate proton transfer [22,31]. It is well known that the addition of tungsten oxide can enhance CO tolerance, and improve the stability and activity of catalysts.



Zhang et al. prepared Pt-WO₃/C catalysts by loading Pt on WO₃ modified carbon. Their results indicated that the catalytic activity of Pt-WO₃/C catalysts for EOR increased with increasing WO₃ content [27].

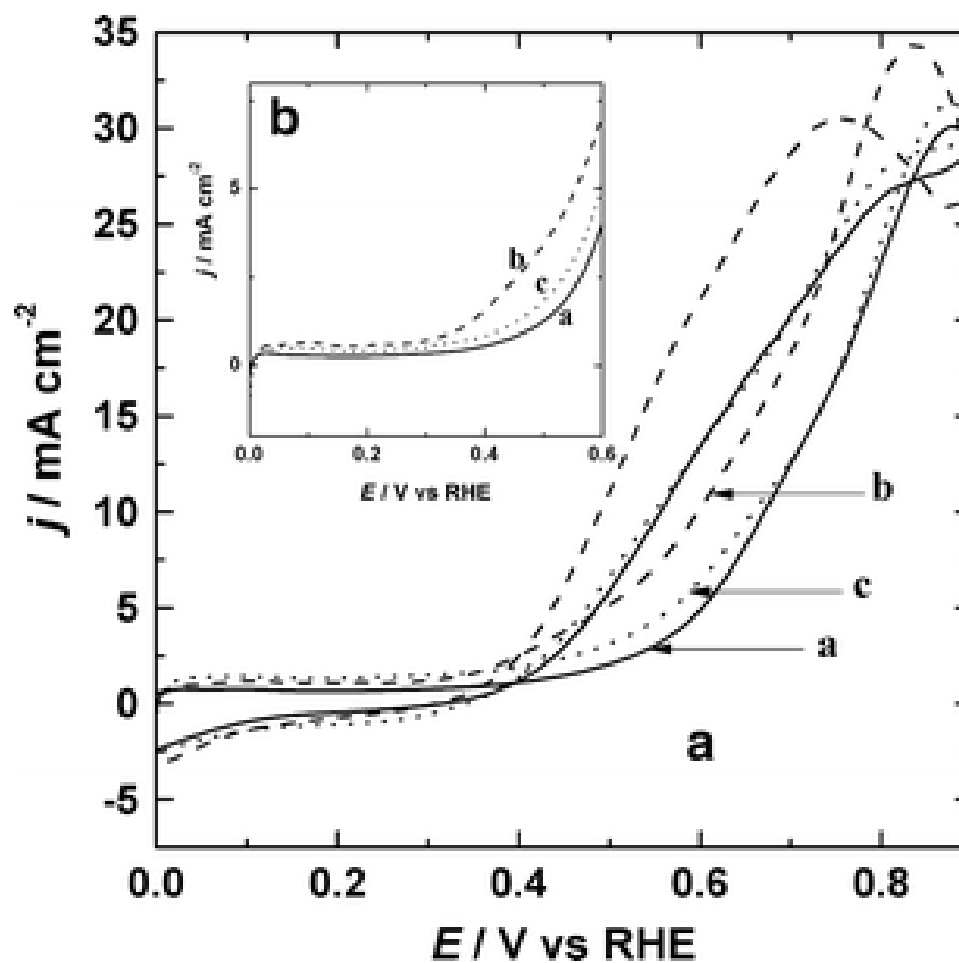


Figure 1.6: A. Cyclic voltammograms (10 mV/s) of (a) PtRh/C, (b) MoO₃-modified PtRh/C and (c) WO₃-modified PtRh/C catalysts in 0.5 M H₂SO₄ (aq) containing 0.5 M ethanol. B. Linear sweep voltammograms (10 mV/s) of (a) PtRh/C, (b) MoO₃-modified PtRh/C and (c) WO₃-modified PtRh/C catalysts in 0.5 M H₂SO₄ (aq) containing 0.5 M ethanol. Reprinted from ref. [38].

1.5.3 Molybdenum oxide

Molybdenum can form five Magneli phase oxides with compositions between MoO_2 and MoO_3 . Molybdenum oxides have been considered for use in fuel cells because they are acid-resistant. MoO_2 has a rutile crystal structure and excellent electronic conductivity, while MoO_3 has an orthorhombic crystal structure and is non-conductive. However, similar to WO_3 , MoO_3 is also capable of forming a non-stoichiometric and electro-conductive hydrogen molybdenum bronze (H_xMoO_3). It has been reported that the presence of molybdenum oxide can enhance the catalytic activity and stability of Pt due to strong electronic interactions between Pt and molybdenum oxide [34,35].

Miecznikowski reported that the addition of MoO_3 or WO_3 to PtPh/C favors the electro-oxidation of ethanol at a low potential (as shown in Figure 1.6). Both MoO_3 modified and WO_3 modified PtRh/C catalysts exhibited better CO tolerance and higher catalytic activity compared with PtRh/C. In terms of the CV results, MoO_3 modified PtRh/C was the best catalyst compared to WO_3 modified PtRh/C and unmodified PtRh/C [38].

1.5.4 Tin oxide

Tin(IV) oxide (SnO_2) is an n-type semiconductor. Compared with TiO_2 , SnO_2 has higher electrical conductivity and a lower price [35]. Although SnO_2 shows good co-catalytic activity for EOR, it is not very stable under fuel cell conditions. Hence, it is often doped with other metals to improve its stability and enhance its electrical conductivity [22, 34]. Jiang et al. prepared a Pt SnO_2 /C catalyst and found that its performance in a DEFC was superior to a commercial Pt/C catalyst [39]. As shown in Figure 1.7, the incorporation of SnO_2 greatly enhanced the catalytic activities of Pt/C and PtRh/C for EOR at low potentials [40].

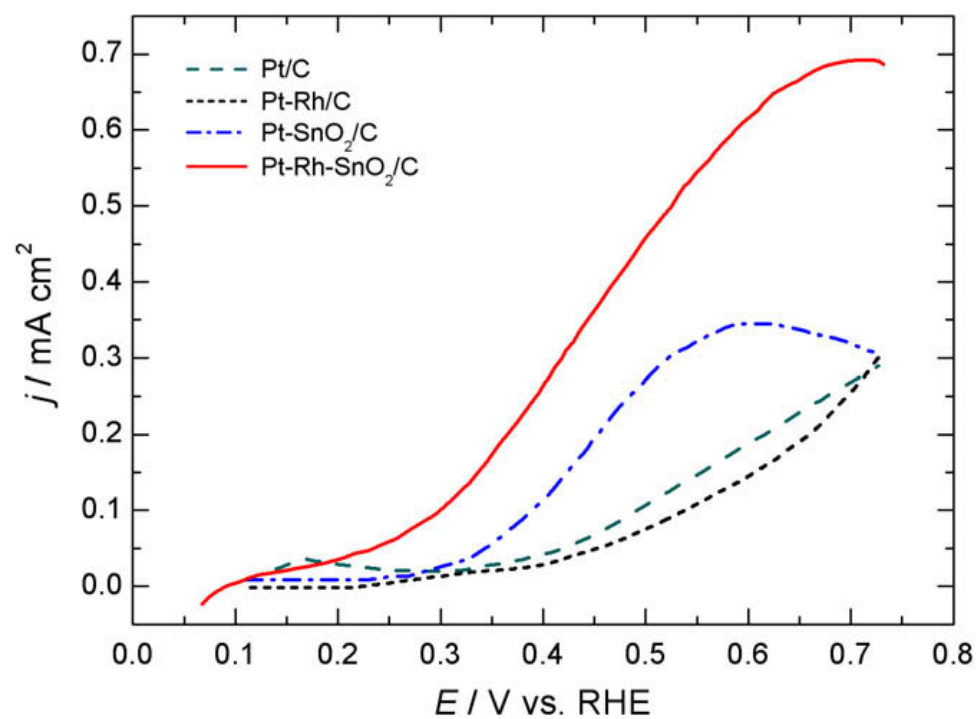


Figure 1.7: Potentiodynamic polarization curves of ethanol electro-oxidation in 0.5 M H_2SO_4 (aq) containing 1 M ethanol on different catalysts. Scan rate 50 mV/s, temperature 20 °C. Reprinted from ref. [40]. Copyright 2009, with permission from Elsevier.

1.5.5 Ruthenium oxide

Ruthenium(IV) oxide (RuO_2) is the most common oxide of ruthenium and is highly electrically conductive. Hydrous ruthenium oxide is an excellent mixed proton-electron conductor with a high specific capacitance [41,42]. Peng et al. reported that the presence of ruthenium oxide in Pt/CNTs improved the CO tolerance and promoted a uniform distribution of Pt nanoparticles on CNTs [43]. Calegaro et al. found that the onset potential of EOR shifted to a less positive value when the RuO_2 was incorporated into Pt/C. A Pt- RuO_2 - IrO_2 /C catalyst, prepared by co-deposition of RuO_2 and IrO_2 into Pt/C, showed the best catalytic activity compared with Pt/C, Pt-Ru/C and Pt- RuO_2 /C [44]. Moghaddam and Pickup investigated the support effects of different oxides on EOR at Pt nanoparticles. They found that tin oxide, ruthenium oxide, and ruthenium-tin mixed oxide supports enhanced the performance of EOR. It is worth noting that Pt on tin oxide showed very high initial activities, while Pt on ruthenium-tin mixed oxide exhibited a more stable performance [45].

1.6 Objectives of this thesis

The ultimate objective of this work is to develop a novel DEFC anode catalyst with low cost, high activity and long durability. Our work is aimed at increasing the power density and voltage efficiency, without loss of faradaic efficiency. In this thesis, the main focus is to investigate the support effect of Ru-Sn oxide modified C (RuSnO_2/C) on Pt nanoparticles for EOR. The effects of reaction conditions, Ru:Sn:C ratios, Pt loading, and heat treatment have been investigated. To better understand the support effect, an ethanol electrolysis cell (EEC) was used to evaluate the catalysts. Product distributions and faradaic efficiencies were obtained through these EEC experiments.

Chapter 2

Experimental

2.1 Preparation of Catalysts

A series of catalyst supports were prepared by modifying carbon black (Vulcan XC-72) with Ru-Sn mixed oxides. Supported Pt nanoparticle (Pt-RuSnO₂/C) catalysts were prepared to investigate the effect of reaction conditions, Ru:Sn:C ratios, Pt loading, and heat treatment.

2.1.1 Chemicals

The following materials were used for preparing catalysts: carbon black (Vulcan XC-72, Cabot), potassium hydroxide (KOH, ACP Chemical Inc.), potassium perruthenate(VII) (KRuO₄, Alfa Aesar), tin(IV) chloride hydrate (SnCl₄ · xH₂O, Alfa Aesar), dihydrogen hexachloroplatinate(IV) hexahydrate (H₂PtCl₆ · 6 H₂O, Pressure Chemical Co.), sodium citrate (Sigma-Aldrich) and sodium borohydride (NaBH₄, BDH chemicals).

2.1.2 Modifying Carbon Black

Carbon black was modified by deposition of a thin layer of Ru-Sn mixed oxides. KRuO_4 can react with carbon and form ruthenium oxide [46]. SnCl_4 was slowly hydrolyzed in the suspension and the formed hydrous tin oxide which co-deposited onto carbon. RuSnO_2/C (110)* is prepared by using the same method reported in ref. [46], referred to in this thesis as the original method. Various reaction conditions and Ru:Sn:C ratios (Table 2.1) were used in order to optimize the composition and structure of the modified carbon.

In the naming system, * is used to indicate that the reaction time was 30 min. Without the label *, the reaction time was 24 h. As for the numbers in the bracket, the first number, the second number and the third number are related to the KOH concentration used for Ru precursor solution, Sn precursor solution and C suspension, respectively (1 means 0.1 M, 2 means 0.2 M and 0 means 0 M). The same KOH concentration (0.057 M) was used for the support labelled with 0.057. C_{low} means that lower amount of carbon was used for preparing the support(RuSnO_2/C_{low}).

Table 2.1: RuSnO_2/C preparation conditions.

	KRuO_4	$\text{SnCl}_4 \cdot x\text{H}_2\text{O}$	C
RuSnO_2/C (110)* [46]	0.1580 g in 30.0 mL 0.10M KOH	0.2650 g in 30.0 mL 0.10M KOH	0.6986 g in 45.0 mL H_2O
RuSnO_2/C (110)	0.1561 g in 30.0 mL 0.10M KOH	0.2678 g in 30.0 mL 0.10M KOH	0.6500 g in 45.0 mL H_2O
RuSnO_2/C_{low} (110)	0.1181 g in 24.0 mL 0.10M KOH	0.2045 g in 24.0 mL 0.10M KOH	0.0870 g in 10.0 mL H_2O
RuSnO_2/C (0.057)	0.1524 g in 30.0 mL 57mM KOH	0.2653 g in 30.0 mL 57mM KOH	0.5986 g in 45.0 mL 57mM KOH
RuSnO_2/C (222)	0.0780 g in 15.0 mL 0.20M KOH	0.1328 g in 15.0 mL 0.20M KOH	0.3014 g in 22.5 mL 0.20M KOH

*The reaction time was 30 min.

2.1.3 Pt Deposition

Pt nanoparticles were deposited on to the modified C by using a NaBH_4 reduction reaction. Depending on the target Pt loading, different amounts of Pt solution were used. For example, RuSnO_2/C powder (0.2023 g) was dispersed in 30.0 mL of H_2O and was sonicated for 10 min. The Pt solution (0.1820 g of $\text{H}_2\text{PtCl}_6 \cdot 6\text{H}_2\text{O}$ in 10.0 mL of H_2O) was then added drop-wise into the RuSnO_2/C suspension. After 0.5 h mixing, sodium citrate (0.1792 g in 12.0 mL H_2O) solution was added into the mixture and stirred for another 1 h. Finally, the NaBH_4 (0.0898 g in 20 mL H_2O) solution was slowly added to the mixture and allowed to react for 3 h with vigorous stirring. Pt– RuSnO_2/C powder (0.2456 g) was collected by suction filtration, rinsed with distilled water and air-dried overnight.

2.1.4 Heat Treatment

There were two different types of heat treatment. One was the heating RuSnO_2/C supports at 200 °C in air for 12 h (supports heat treatment). The other one was heating Pt– RuSnO_2/C catalysts at 130 °C or 200 °C in air for 1 h (catalysts heat treatment).

2.2 Preparation of Electrodes and MEAs

For the preparation of electrodes and membrane electrode assemblies (MEAs), the following chemicals and materials were used: carbon fiber paper (CFP, TorayTM), glassy carbon (GC) electrode ($\text{Ø}=3.0$ mm), 1-propanol, 2-propanol, Nafion[®] solution (5%, DuPont), alumina polishing suspension (Micro Metallurgical Ltd.), Rayfinal polishing cloth (Micro Metallurgical Ltd.).

For the preparation of catalyst-coated electrodes, 2.0 mg of catalyst was dispersed

in a mixed solution containing 120 μL of H_2O , 30 μL of 1-propanol and 50 μL of Nafion[®] solution and the resulting ink was sonicated for 1 h. Then, 3.0 μL of ink was applied to a glassy carbon electrode previously polished with 0.3 μm alumina and dried at room temperature [47].

For the nine-anode cell experiments, MEAs were prepared by pressing a cathode (4 mg cm^{-2} Pt black) and nine anodes onto a NafionTM 115 membrane in the cell. In the anode preparation, the target loading of Pt was 4 mg cm^{-2} , the target loading of Nafion was 20 wt% and an appropriate amount of 1-propanol was used to disperse the catalyst. The mixture (catalyst, Nafion solution and 1-propanol) was sonicated for 3 h and then painted onto carbon fiber paper. This work was done by Tobias Brueckner.

For the 5 cm^2 cell experiments, the anode (30%Pt-RuSnO₂/C_{low}) was prepared as follows: 10.2 mg of carbon black was dispersed in 100 μL of 1-propanol and 50 μL of 5 wt% Nafion solution and sonicated for 3 h. Carbon fiber paper was coated with this carbon slurry. 41.3 mg of catalyst was dispersed in 80 μL of 1-propanol and 200 μL of 5 wt% Nafion solution and sonicated for 3 h. When the carbon slurry was completely dried, the catalyst slurry was painted onto the top of the carbon layer and dried overnight. MEAs were prepared in the same way as for the multi-anode cell experiments.

2.3 Electrochemical Measurements

A RDE4 analog bipotentiostat (Pine Instrument Company) was used for cyclic voltammetry and chronoamperometry measurements in a three electrode cell which contained a Pt wire counter electrode, a GC working electrode, and a saturated calomel reference electrode (SCE). Some measurements were made using CFP as the working

electrode. A SP-50 Potentiostat (Bio-Logic Science Instruments) was also used for cyclic voltammetry and chronoamperometry measurements.

Polarization curves for the nine-anode cell were measured with an Arbin Instruments multi-channel potentiostat. As shown in Figure 2.1, the cell was operated in crossover mode with 0.1 M ethanol solution pumped into the cathode while N_2 was purged into the anode at a flow rate of 30 mL min^{-1} [48]. Polarization curves of the 5 cm^2 cell were measured with a Potentiostat/Galvanostat HA 301 (Hokuto Denko) and this cell was operated in anode polarization mode (shown in Figure 1.3) where ethanol was pumped into the anode and N_2 was purged into the cathode [13].

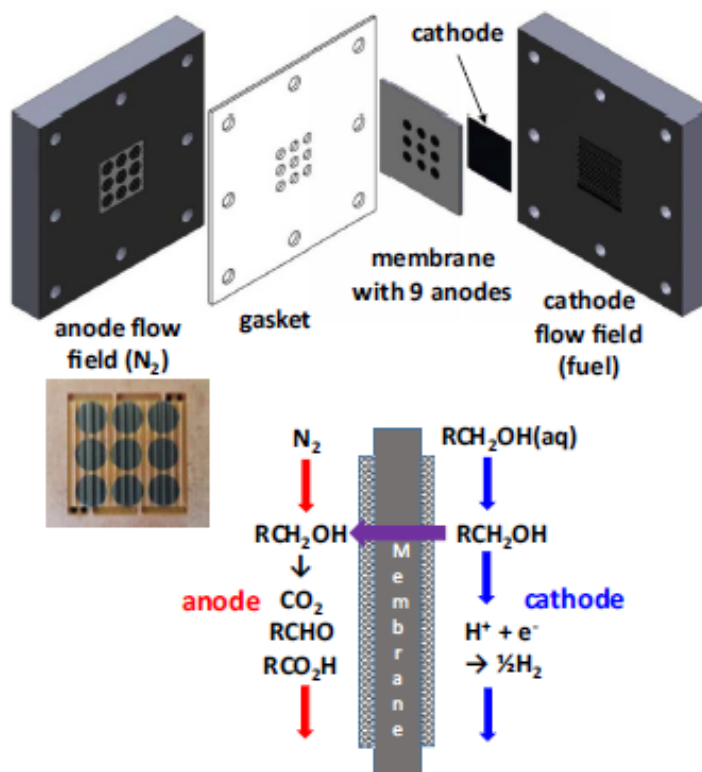


Figure 2.1: Schematic diagram of the nine-anode PEM cell (top) and crossover mode of operation (bottom). $R = \text{CH}_3$. Reprinted from ref. [48].

2.4 Product Distribution Measurements

2.4.1 Non-Dispersive Infrared (NDIR) Carbon Dioxide Detector

A NDIR CO₂ detector is a device for monitoring the concentration of CO₂ by detecting the intensity of transmitted IR light. The principle can be explained by Beer's law (Equations 2.1 and 2.2).

$$I_t = I_0 * 10^{-A} \quad (2.1)$$

where I_t is the intensity of transmitted light, I_0 is the intensity of incident light, and A is absorbance.

$$A = \epsilon * c * l \quad (2.2)$$

where ϵ is molar extinction coefficient, c is the molar concentration of CO₂ and l is the thickness of the absorbing medium.

CO₂ measurements were made with a commercial Telaire 7001 CO₂ detector and recorded by Logger Pro software.

2.4.2 Nuclear Magnetic Resonance (NMR) Spectroscopy

NMR is a qualitative and quantitative technique in which the magnetic properties of specific nuclei are investigated. By using NMR in our experiments, ethanol (EtOH), acetic acid and acetaldehyde can be identified and their concentration can be measured. Combined with the CO₂ detector, a full product distribution can be obtained.

NMR experiments were conducted on a Bruker AVANCE III 300 spectrometer. 400 μ L of sample (products and residual ethanol in H₂O) was mixed with 100 μ L of D₂O containing 32 mM fumaric acid before NMR analysis. The peak area in NMR is proportional to the concentration of each analyte. The unknown concentration of

analytes (AA, AAL, and EtOH) can be calculated by comparing their peak areas with fumaric acid's (6.4 mM) peak area.

2.5 Catalyst Characterization

2.5.1 Thermogravimetric Analysis (TGA)

TGA is an analytical technique in which the temperature is increased over time and the mass is measured as a function of temperature. The total metal loading of our catalysts can be easily obtained by TGA since the boiling point of Pt, Ru oxide and tin oxide are above the maximum temperature and they are thermally stable over the operation temperature range.

TGA experiments were conducted on a TA instruments Q500 thermogravimetric analyzer. Thermal Advantage software was used for processing raw data. The scan rate was $20\text{ }^{\circ}\text{C min}^{-1}$ and the temperature range was from ambient temperature to $800\text{ }^{\circ}\text{C}$. Most experiments were conducted under an air atmosphere and some of them were conducted under N_2 . The TGA platinum sample pan was stored in 3 M HCl solution. Before each experiment, the pan was rinsed with copious amount of de-ionized water and then torched with a propane burner. The sample size was about 5 mg.

2.5.2 X-Ray Diffraction (XRD)

XRD is a powerful and non-destructive technique which can yield information regarding the crystal structure, composition, and particle size of our catalysts.

The catalyst powder was characterized with a Rigaku Ultima IV X-ray diffractometer using Cu-K_{α} radiation (1.5418 \AA) at a power of 40 kV and 44 mA. Continuous

scanning was used from 20° to 90° in 2 with a 0.02° step size. This work was done by Dr. Wanda Aylward in the Earth Science department at Memorial University.

2.5.3 Inductively Coupled Plasma Optical Emission Spectroscopy (ICP-OES)

ICP-OES is a qualitative and quantitative multi-element analysis method. The sample solution was aspirated with argon gas into a plasma to produce excited atoms and ions which emit characteristic spectra. The intensity of emission is proportional to the concentration of each element.

ICP-OES measurements were carried out using a Perkin Elmer 5300 DV inductively coupled plasma–optical emission spectrometer by Adam Beaton. To dissolve the metals from the catalyst samples, 8 mL of aqua regia was added to about 6 mg of the sample in a 15 mL perfluoroalkoxy alkane (PFA) vial with a 33 mm PFA closure. The mixture was heated at 65 °C for 20 h and then residual carbon black was removed with a syringe filter. Extra water was used to collect the solution left in the vial, syringe, and filter. The filtrate was finally diluted to 15.0 mL by water before ICP-OES analysis. Calibration curves were prepared by using commercial standard Pt, Ru, and Sn solutions.

2.5.4 Scanning Electron Microscopy (SEM) with Energy Dispersive X-Ray Analysis (EDX)

SEM is one type of electron microscopy which is capable of surface analysis. By applying focused scanning electron beams to the sample surface, the secondary, or backscattered electron signals are produced which can provide high resolution images. The characteristic X-ray radiation backscattered from the sample can be measured

by EDX analyzer which gives qualitative and semi-quantitative information about the elemental composition.

SEM-EDX analysis was carried out using Quanta 400 SEM with Roentec SDD EDX X-ray detectors by Dr. David Grant. About 5 mg of catalyst powder was dispersed in 300 μL of 2-propanol and sonicated for 3 h. Then, the ink was applied to an adhesive carbon tab on the specimen stub.

2.5.5 Transmission Electron Microscopy (TEM)

TEM is another electron microscopy which can provide extremely high resolution images. Different to SEM, the electron beam is transmitted through the thin layer specimen. In addition to the particle size, element distribution and semi-quantitative information can be obtained when TEM is coupled with an Energy Dispersive X-ray system.

TEM analysis was conducted on a JEOL 2011 scanning transmission electron microscope at University of New Brunswick by Steven Cogswell. The sample was dispersed in anhydrous ethanol and sonicated. A drop of ink was applied onto the carbon suspension film coated TEM grid. Elemental analysis was carried out with EDAX (Genesis) Energy Dispersive X-ray system.

Chapter 3

Characterization of the Supports and Catalysts

3.1 TGA

To investigate the best conditions for preparing Ru-Sn oxide modified C supports, TGA analysis was first carried out. The residue was assumed to be RuO_2 and SnO_2 because both of them are thermally stable and have boiling points higher than $1000\text{ }^\circ\text{C}$. As shown in Figure 3.1, the weight loss before $200\text{ }^\circ\text{C}$ (where carbon will not easily be oxidized under N_2) suggests that the Ru and Sn oxide in this RuSnO_2/C (110) support were hydrous. Based on the estimation of mass loss, metal oxide is assumed to be present as $\text{MO}_2 \cdot \text{H}_2\text{O}$. Following heat treatment at $200\text{ }^\circ\text{C}$, the RuSnO_2/C (110) support had less mass loss at low temperature and a much higher residual mass than the as-prepared RuSnO_2/C (110) support, which suggests that the hydrous oxide was dehydrated and some carbon was oxidized at $200\text{ }^\circ\text{C}$. Residual masses for the other supports are presented in Table 3.1.

The target values for RuO_2 and SnO_2 were based on the initial preparation condi-

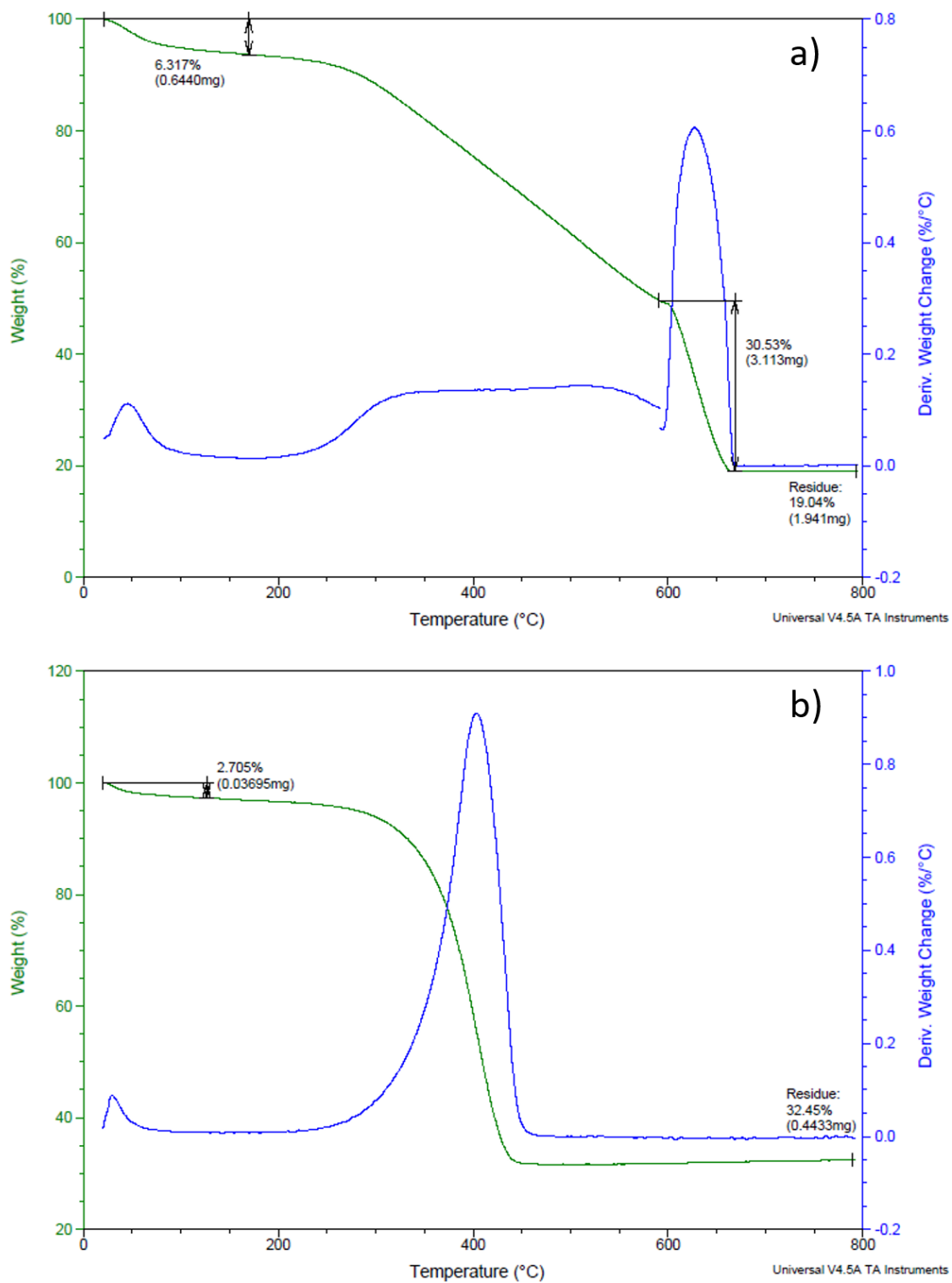


Figure 3.1: TGA analysis of (a) as-prepared RuSnO₂/C (110), N₂ gas was switched to air at 600 °C, and (b) RuSnO₂/C (110) heated at 200 °C for 20 h, air was used all the time.

tions. Based on the assumption that the hydrolysis of SnCl_4 and the redox reaction between C and KRuO_4 were complete, the target loading of oxide can be calculated (shown in Table 3.1). By comparing the target RuSnO_2 ($\text{RuO}_2 + \text{SnO}_2$) value with the TGA residue, the extent of reaction can be estimated.

Table 3.1: TGA results: the effect of reaction time, conditions and carbon content.

Support	Target		RuSnO ₂ %	Found Residue%
	RuO ₂ %	SnO ₂ %		
Original method [46]				
RuSnO ₂ /C (110)*	11.00	12.17	23.17	14.53
Different compositions				
RuO ₂ /C (110)	14.09	0	14.09	17.08
SnO ₂ /C (110)	0	15.76	15.76	1.19
RuSnO ₂ /C (110)	11.46	12.97	24.43	19.04
Different KOH concentration				
RuSnO ₂ /C (222)	12.12	13.61	25.72	18.30
RuSnO ₂ /C (0.057)	11.93	13.70	25.64	20.19
RuSnO ₂ /C (100)	12.05	13.69	25.74	27.27
RuSnO ₂ /C (000)	12.00	13.63	25.63	25.00
Different carbon content				
RuSnO ₂ /C _{low} (110)	28.76	32.85	61.61	45.23

*The reaction time was 30 min in the original method and 24 h for others. The metal oxide was assumed to be present as $\text{MO}_2 \cdot \text{H}_2\text{O}$.

The TGA residue of RuO_2 for the RuO_2/C (110) sample was higher than the target value which may be because of the loss of C during filtration (The weighed C was washed with 0.1 M H_2SO_4 before use), impurities from the C and KRuO_4 , or the assumption of $\text{MO}_2 \cdot \text{H}_2\text{O}$ (if each MO_2 contained less H_2O , the calculated target value will be higher). The TGA residue of SnO_2 for the SnO_2/C (110) sample was much lower than the target value, which indicates that 0.057 M KOH in this reaction mixture was not suitable for the deposition of SnO_2 . When comparing RuSnO_2/C supports prepared under different KOH concentrations, it can be seen that the supports prepared under less basic conditions have higher residue values. The difference of residue values is likely due to the varying degrees of SnO_2 deposition (It was confirmed

by the ICP-OES results later (shown in Table 3.2). In the preparation of RuSnO₂/C (000), when the KRuO₄ and SnCl₄ were dissolved in water without any base, a black precipitate was formed which can be attributed to reduction of KRuO₄ by water. Although this support had a higher amount of SnO₂ (it was confirmed by ICP-OES that its Pt-based catalyst had a higher amount of SnO₂ than others), its Pt-based catalyst did not perform well in cyclic voltammograms as shown in Chapter 4. In general, the TGA results indicate that oxide deposition was almost quantitative when the KOH concentration was less than 0.057 M, while SnO₂ deposition was incomplete at 0.057 M and higher concentrations. Better understanding of the composition of the catalysts requires elemental analysis such as XRF, SEM-EDX, and ICP-OES.

3.2 XRD

It is expected that the main crystalline components of RuSnO₂/C are RuO₂ and SnO₂. XRD was used to investigate the phases of RuO₂ and SnO₂. However, as shown in Figure 3.2, it is hard to find peaks of RuO₂ and SnO₂ in the as-prepared RuSnO₂/C (110), which may be because RuO₂ and SnO₂ in the support were mainly amorphous and the amorphous phases will not be observed by XRD. Hence, the as-prepared RuSnO₂/C (110) was heated at 200 °C to increase the degree of crystallization. By comparing the XRD patterns of the as-prepared sample and sample after heating, the structure of RuO₂ and SnO₂ can be well understood.

In Figure 3.2, the peak positions for the RuO₂ and SnO₂ crystal planes are shown by the dashed lines. The tetragonal RuO₂ has main peaks at 27.9°, 34.9°, and 54.0° which are associated with the (110), (101), and (211) planes, respectively (ICSD PDF: 03-065-2824). As for tetragonal SnO₂, its main peaks are at 26.6°, 33.8°, 37.9°, 51.7° and 64.7° which are associated with the (110), (101), (200), (211), and (112) planes,

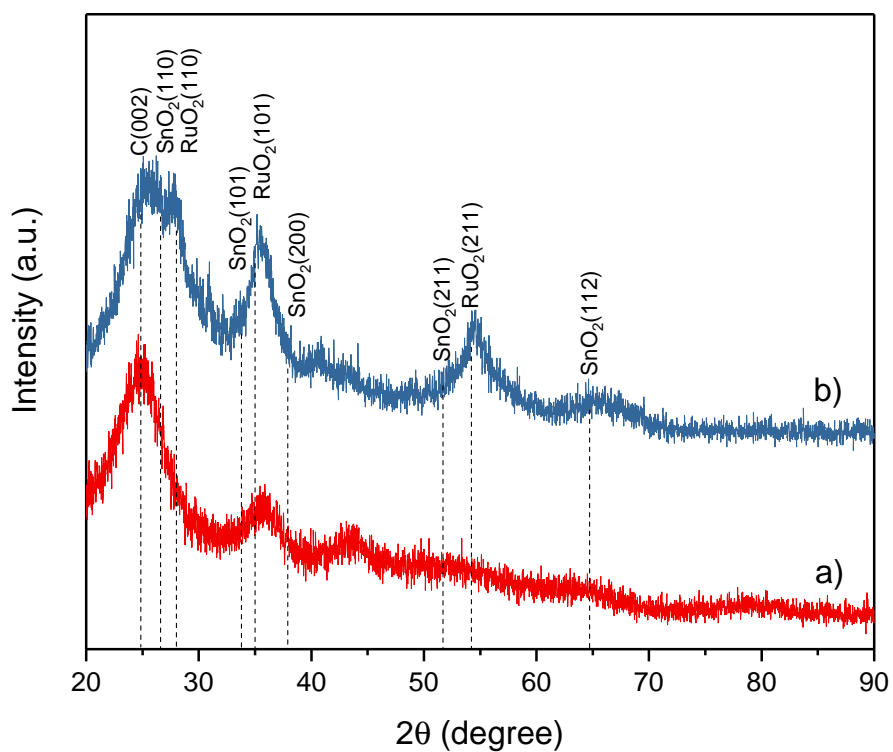


Figure 3.2: XRD patterns of (a) as-prepared RuSnO_2/C (110), and (b) RuSnO_2/C (110) heated at 200 °C for 20 h.

respectively [49].

The as-prepared RuSnO₂/C (110) has a broad and small peak at ca. 35.5° which suggests the presence of crystalline RuO₂. After heat treatment, this peak became sharper and more intense, and peaks at ca. 28.0°, 54.6° and 65.0° appeared because more amorphous RuO₂ became more crystalline. The peak of C(002) is dominant in both of these XRD patterns, which makes it difficult to observe the SnO₂(110) and RuO₂(110) peaks. In addition, the peaks at ca. 41.0° are from the carbon supports (Vulcan XC-72) [50].

As discussed in Chapter 2, the catalyst supports were prepared under different pH conditions while the deposition method for Pt onto the supports was the same. By using XRD, the structure of the Pt nanoparticles and the presence of crystalline SnO₂ and RuO₂ can be investigated. Figure 3.3 shows XRD patterns for 25%Pt-RuSnO₂/C (0.057), 25%Pt-RuSnO₂/C (0.057), and 25%Pt-RuSnO₂/C (222).

In Figure 3.3, the peaks at ca. 39.8°, 46.3°, 67.8°, 81.4°, and 86.1° are due to the Pt(110), Pt(200), Pt(220), Pt(311) and Pt(222) planes, respectively. There are no obvious shifts of these Pt peaks which indicates that Pt deposition was not influenced by the supports and no alloys (such as PtRu and PtSn) were formed. The first peak of (c) 25%Pt-RuSnO₂/C (222) at ca. 25.0° is due to the C(002) plane. However, the first peaks of (b) 25%Pt-RuSnO₂/C (0.057) and (a) 25%Pt-RuSnO₂/C (000) are slightly shifted to the right which may be due to overlapping of SnO₂(110) peaks. In addition, the peaks of (a) 25%Pt-RuSnO₂/C (000) at ca. 33.8° and 51.7° are due to the SnO₂(101) plane and SnO₂(211) plane, respectively [49]. The broadness and low intensity of these SnO₂ peaks suggests that the crystalline SnO₂ has a very small particle size and is well dispersed or SnO₂ is poorly crystalline. No crystalline RuO₂ peaks are found in any of these three catalysts.

Figure 3.4 shows the XRD patterns of (a) 25%Pt-RuSnO₂/C (110), (b) 25%Pt-

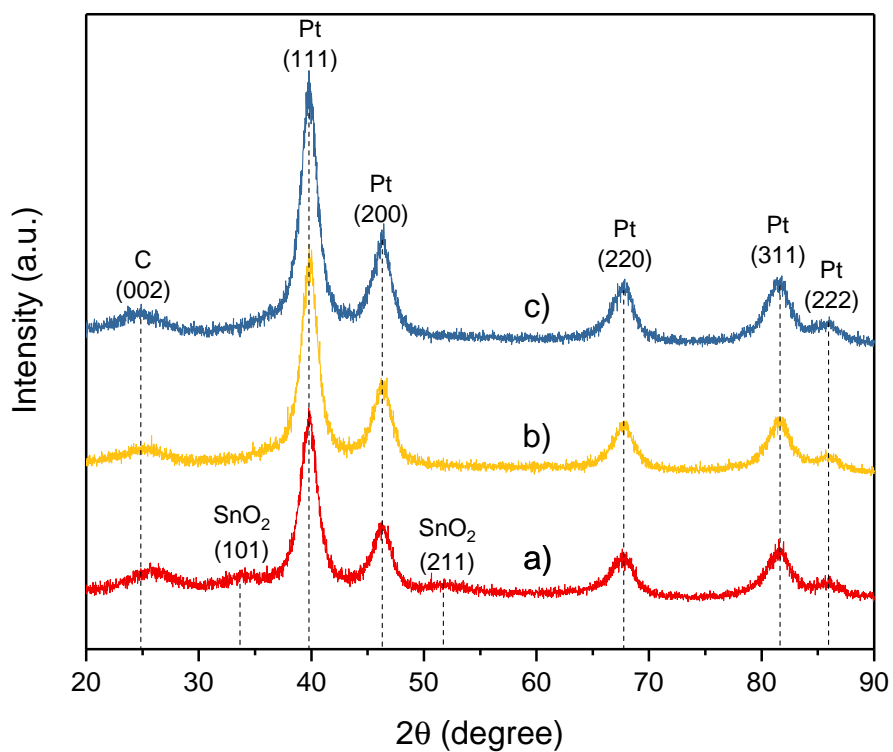


Figure 3.3: XRD patterns of (a) 25%Pt-RuSnO₂/C (000), (b) 25%Pt-RuSnO₂/C (057), and (c) 25%Pt-RuSnO₂/C (222).

RuSnO₂/C (110)*, and (c) 70%Pt-RuSnO₂/C (110). These catalysts not only have almost the same Pt peak positions as each other, but also have the same Pt peak positions compared to those in Figure 3.3, which further confirmed that the structure of the Pt crystals was not influenced by the preparation of RuSnO₂/C supports under different conditions (* means that the reaction time between carbon black and Ru-Sn mixed solution was 30 min and the reaction time for other supports was 24 h). There are no obvious peaks associated with crystalline RuO₂ and SnO₂ which suggests that the oxides were either absent or amorphous or the Pt was considerably more crystalline or bigger particles. In 70%Pt-RuSnO₂/C (110), the carbon (002) peak was absent which maybe due to the high coverage of Pt nanoparticles.

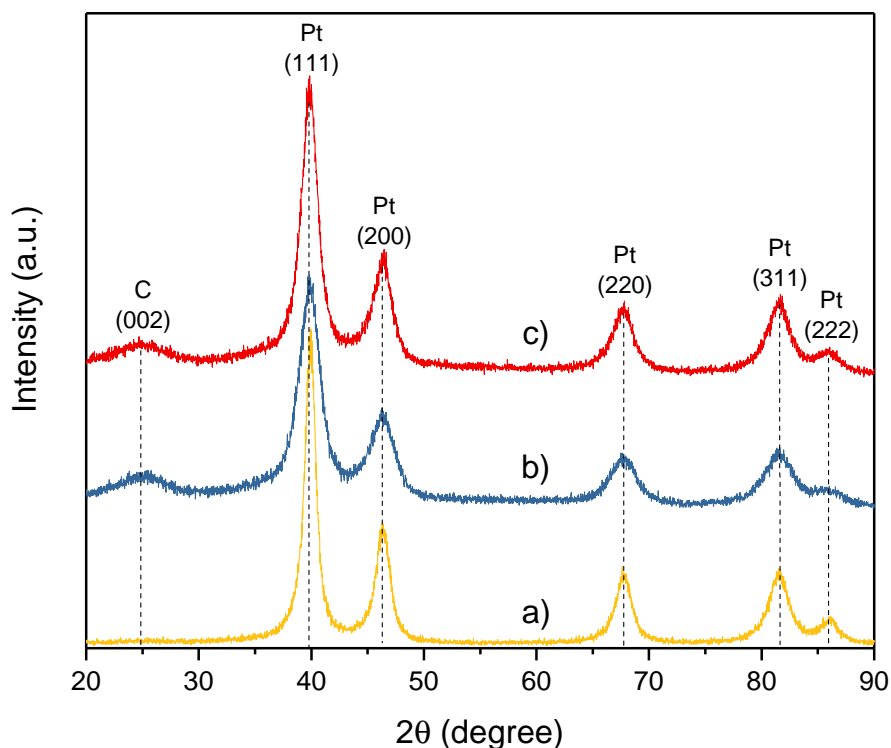


Figure 3.4: XRD patterns for (a) 70%Pt-RuSnO₂/C (110), (b) 25%Pt-RuSnO₂/C (110)*, and (c) 25%Pt-RuSnO₂/C (110).

3.3 ICP-OES

As shown in Table 3.2, 25%Pt-RuSnO₂/C (000) has the highest amount of Sn which indicates that the deposition of SnO₂ requires less basic conditions. 25%Pt-RuSnO₂/C (110) has a higher amount of Ru than 25%Pt-RuSnO₂/C (110)* which indicates that the reaction between C and KRuO₄ takes longer than 30 min. The Ru content of the other 25%Pt catalysts, with same reaction time but different pH conditions, was similar which means that the deposition of RuO₂ is mainly determined by the reaction time rather than by pH.

All the 25%Pt catalysts should have ca. 25% Pt based on the amount of H₂PtCl₆ · 6H₂O used. However, there were some assumptions for the calculation. First, H₂PtCl₆ · xH₂O was assumed to be present as H₂PtCl₆ · 6H₂O and to be totally reduced to Pt in the reaction. Second, it is assumed that the water content of the original support (RuSnO₂/C) would be retained which means the ratio of (RuO₂+SnO₂+C) to H₂O in RuSnO₂/C is the same as that in Pt-RuSnO₂/C. Hence, if the RuSnO₂/C used for preparing Pt-RuSnO₂/C was not dried enough and the as-prepared Pt-RuSnO₂/C was dried properly, then the measured Pt% would be higher than we expect. This may explain the high Pt contents measured for 25%Pt-RuSnO₂/C (110) and 25%Pt-RuSnO₂/C (000).

It is worth noting that the digestion of the catalysts requires some specific conditions. Pt can be easily dissolved in aqua regia with or without heating based on our experiments. However, digesting the hydrous RuO₂ in Pt-RuSnO₂ requires the proper temperature. Digestion of the catalysts at room temperature gave a Ru% value that was about half of the value obtained with heating at ca. 65 °C. Although the metallic elements were largely dissolved with proper heating, the SEM-EDX results (Appendix A.1) showed that some Ru and Sn (mainly Ru) still remained in the carbon residue. Combined with the TGA result, it can be roughly estimated that ca.

Table 3.2: Catalyst composition.

Catalyst	TGA		ICP-OES			
	Pt%	RuSnO ₂ %	Pt%	Ru%	Sn%	RuSnO ₂ %
25%Pt-RuSnO ₂ /C (110)	24.84	14.31	28.3	7.35	1.13	11.12
25%Pt-RuSnO ₂ /C (110)*	24.48	10.97	24.9	5.59	1.13	8.80
25%Pt-RuSnO ₂ /C (000)	26.69	18.33	30.5	5.28	7.43	16.67
25%Pt-RuSnO ₂ /C (0.057)	23.56	15.43	24.9	6.49	0.98	9.78
25%Pt-RuSnO ₂ /C (222)	24.60	13.80	23.6	6.46	0.10	8.63
30%Pt-RuSnO ₂ /C _{low} (110)	32.63	26.98	30.2	17.0	1.20	23.87
70%Pt-RuSnO ₂ /C (110)	68.18	6.06	67.4	2.57	0.57	4.10

RuSnO₂% in ICP-OES was calculated by using Ru% and Sn%.

TGA results were calculated by using the residue (wt%) of supports and catalysts.

It was assumed that the composition of the support did not change.

10 wt% of Ru from the original sample was not dissolved.

3.4 SEM-EDX

In SEM, the distribution of elements can be identified by differences in brightness since different elements have different electron densities and will give different brightness. Normally, the heavier elements will give brighter images. In Pt-RuSnO₂/C, Pt is the heaviest and Sn is heavier than Ru. Therefore, three kinds of brightness can be seen in the image if these three metals are distributed individually. However, as shown in Figure 3.5 (a), only two kinds of brightness (white and grey) were observed in addition to the black background. EDX analysis was applied to obtain qualitative and semi-quantitative information on the catalyst composition. For 25%Pt-RuSnO₂/C (110), it can be seen that Pt, Ru and Sn were found in both the white areas and grey areas as shown in Figure 3.5 (c) and (d). The white area had more Pt% than the grey area, which suggests that the white dots were due to the agglomeration of Pt nanoparticles. For 70%Pt-RuSnO₂/C (110), Figure 3.5 (b), the image was almost white, which suggests that the agglomeration of Pt was much more severe which was

confirmed by its EDX analysis (Figure 3.5 (e)). Detailed EDX analysis results are presented in Table 3.3.

Compared to Figure 3.5 (a), Figure 3.6 (a) for 30%Pt-RuSnO₂/C_{low} (110) shows a relatively consistent color except the black background, which suggests that the thin oxide layer fully covered the carbon surface. In addition, although 30%Pt-RuSnO₂/C_{low} (110) (30.2% Pt according to ICP-OES) has more Pt% than 25%Pt-RuSnO₂/C (110) (28.3% Pt according to ICP-OES), there were no obvious white dots in its SEM image, which suggests that Pt dispersed better in this 30%-RuSnO₂/C_{low} (110) than in 25%-RuSnO₂/C (110). It is worth noting that the catalyst existed as chunks in Figure 3.6, which restricted the observation of inner structure and element distribution and may cause a misconception of this catalyst.

To better understand the Pt dispersion, the ratio of Pt to RuSnO₂ is reported in Table 3.3. It is assumed that a high ratio of Pt to RuSnO₂ (relative to the value from TGA or ICP-OES, which provide averages over many particles, indicates that the Pt was not well dispersed) indicates worse Pt dispersion. The ratio from ICP-OES may be slightly higher than the actual ratio because of the underestimation of Ru (see Section 3.3). The ratio from TGA may be lower than the actual ratio because of the assumptions (see in Section 3.1). Therefore, the actual ratio was assumed to be between the values from TGA and ICP-OES. For 25%Pt-RuSnO₂/C (110), the grey dots and grey areas gave Pt to RuSnO₂ ratio that were quite close to actual ratio, which indicates that most of the Pt was well dispersed and only a small portion of the Pt was agglomerated. As for 70%Pt-RuSnO₂/C (110), the ratio from EDX was much higher than the actual ratio which may be due to high Pt agglomeration where the RuSnO₂ modified C surface was blocked. The Pt layer can absorb the electron beam before it reaches the RuSnO₂ layer and therefore cause the Ru and Sn X-ray intensities to be much lower. As for 30%Pt-RuSnO₂/C_{low} (110), the ratio from EDX

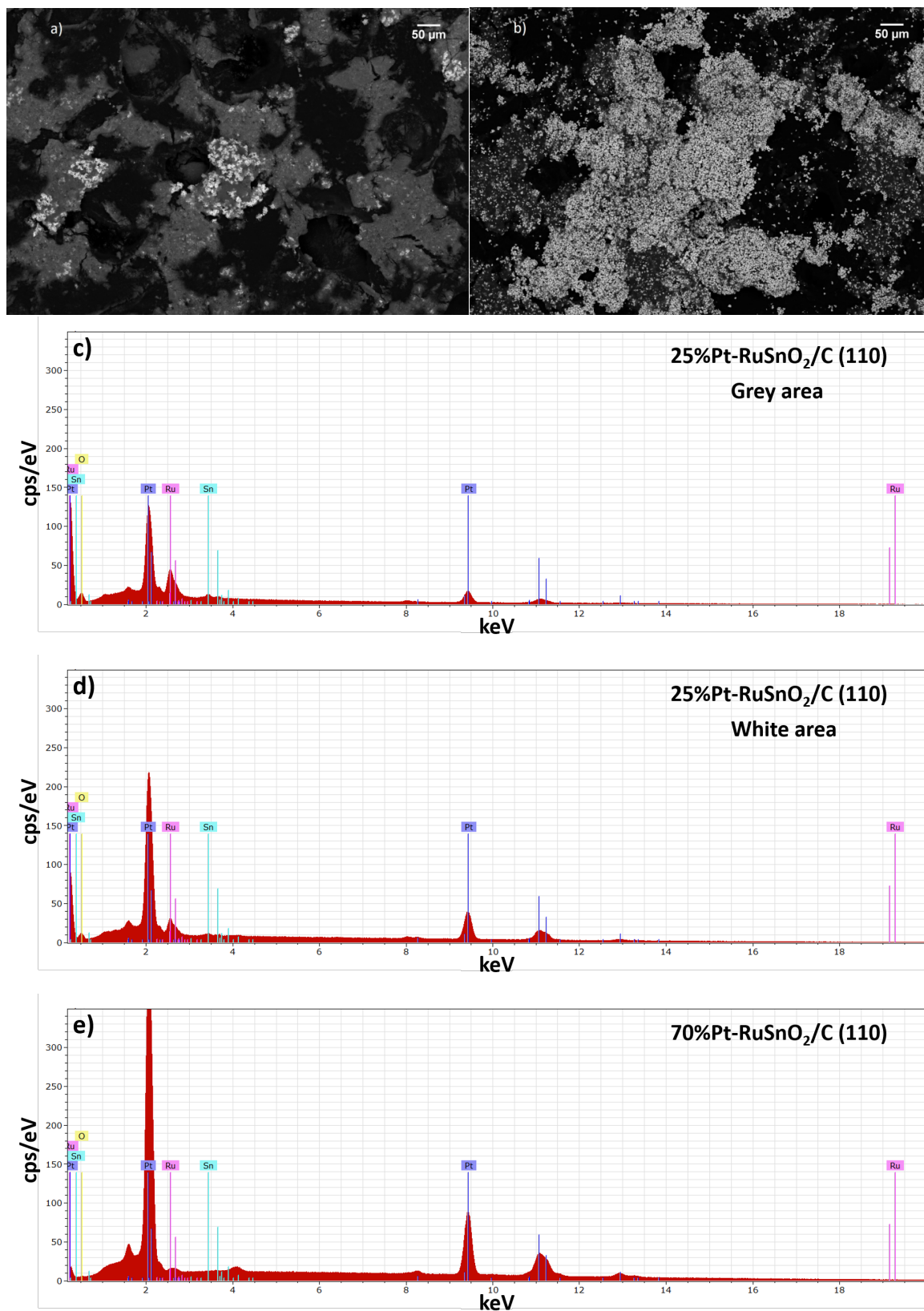


Figure 3.5: SEM images and EDX spectra of 25%Pt-RuSnO₂/C (110) (a, c and d) and 70%Pt-RuSnO₂/C (110) (b and e).

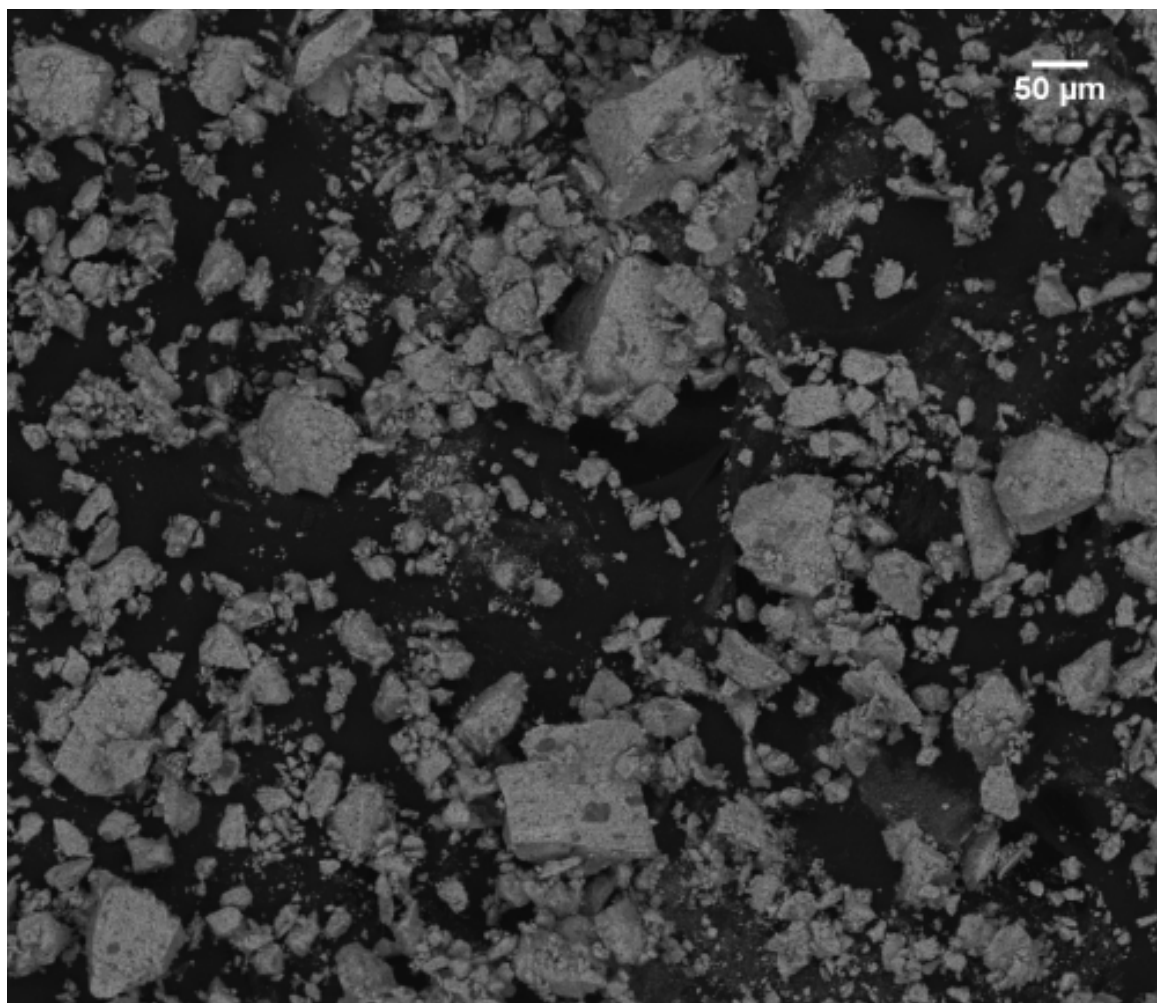


Figure 3.6: SEM image of 30%Pt-RuSnO₂/C_{low} (110).

was really close to the actual ratio, which suggests that Pt was dispersed well in this catalyst.

Table 3.3: SEM-EDX analysis results.

		Pt%	Ru%	Sn%	RuSnO ₂ %	Pt:RuSnO ₂
25%Pt-RuSnO₂/C (110)						
SEM-EDX	White dot 1	65.9	3.9	1.4	7.7	8.5
	White dot 2	61.4	4.4	1.8	9.0	6.8
	White area	49.7	6.2	1.7	11.5	4.3
	Grey dot 1	39.4	11.1	3.0	20.7	1.9
	Grey dot 2	33.6	10.3	2.8	19.2	2.0
	Grey area	30.1	8.4	2.4	15.8	1.9
TGA		24.8	N/A	N/A	14.3	1.7
ICP-OES		28.3	7.4	1.1	11.1	2.5
70%Pt-RuSnO₂/C (110)						
SEM-EDX	Dot 1	71.6	0.1	0	0.1	614.1
	Dot 2	66.0	0.7	0.2	1.3	52.5
	Area 1	72.9	0.2	0.2	0.6	124.5
	Area 2	68.4	0.6	0.2	1.2	57.5
TGA		68.2	N/A	N/A	6.1	11.3
ICP-OES		67.4	2.6	0.6	4.1	16.4
30%Pt-RuSnO₂/C_{low} (110)						
SEM-EDX	Dot	44.2	27.5	2.2	43.6	1.0
	Area	43.0	25.2	2.2	40.3	1.1
TGA		32.6	N/A	N/A	27.0	1.2
ICP-OES		30.2	17.0	1.2	23.9	1.3

SEM-EDX analysis results were semi-quantitative.

RuSnO₂% was calculated by using Ru% and Sn%.

In general, the preparation of RuSnO₂/C requires a lower amount of C or higher amount of Ru and Sn compounds to archive a more complete coverage of the oxide layer. The higher coverage of Ru-Sn oxide helps Pt dispersed better. However, use of a high Pt loading caused a severe Pt agglomeration.

3.5 TEM

Restricted by the resolution, no individual nanoparticles were observed by SEM. Hence, TEM was carried out. As shown in Figure 3.7, there were a lot of individual particles. The average diameter of the Pt nanoparticles was 4.2 ± 0.8 nm (over 50 particles were used for this calculation as shown in Figure C.5). Coupled with a HAADF STEM unit, EDX analysis was carried out to investigate the composition and the circled areas were analyzed. In the EDX spectra which are shown in Appendix C, Pt, Ru and Sn were all found while their ratio varied. Figure C.3 (the circled area in Figure 3.7 (c)) shows high Pt intensity and some Ru and Sn signals. However, in Figure C.4 (the circled area in Figure 3.7 (d)), Ru peaks were dominant and Pt peaks were hardly seen. The EDX spectrum (shown in Figure C.2) related to the circled area in Figure 3.7 (b) shows an intermediate Pt:oxide ratio. Therefore, it can be concluded that the particles were Pt and the fuzzy area was mainly amorphous Ru oxide with a small amount of Sn oxide.

Although the HAADF image (Figure 3.8 (b)) should show atomic contrast by the brightness, the thickness and crystallinity of the sample also influence brightness. Hence, a line scan was used here to investigate the distribution of elements. As shown in Figure 3.8 (d), the signal tendencies were similar for O, Ru and Sn, which once again indicates that Ru and Sn were present as oxide forms in the catalysts and that the co-deposition of Ru oxide and Sn oxide worked well. The Ru and Sn signals also followed the C signal to some extent, although deviations show that the C surface may not have been evenly coated with Ru oxide and Sn oxide. Probably, this phenomenon is an artifact caused by the varying thickness of the sample.

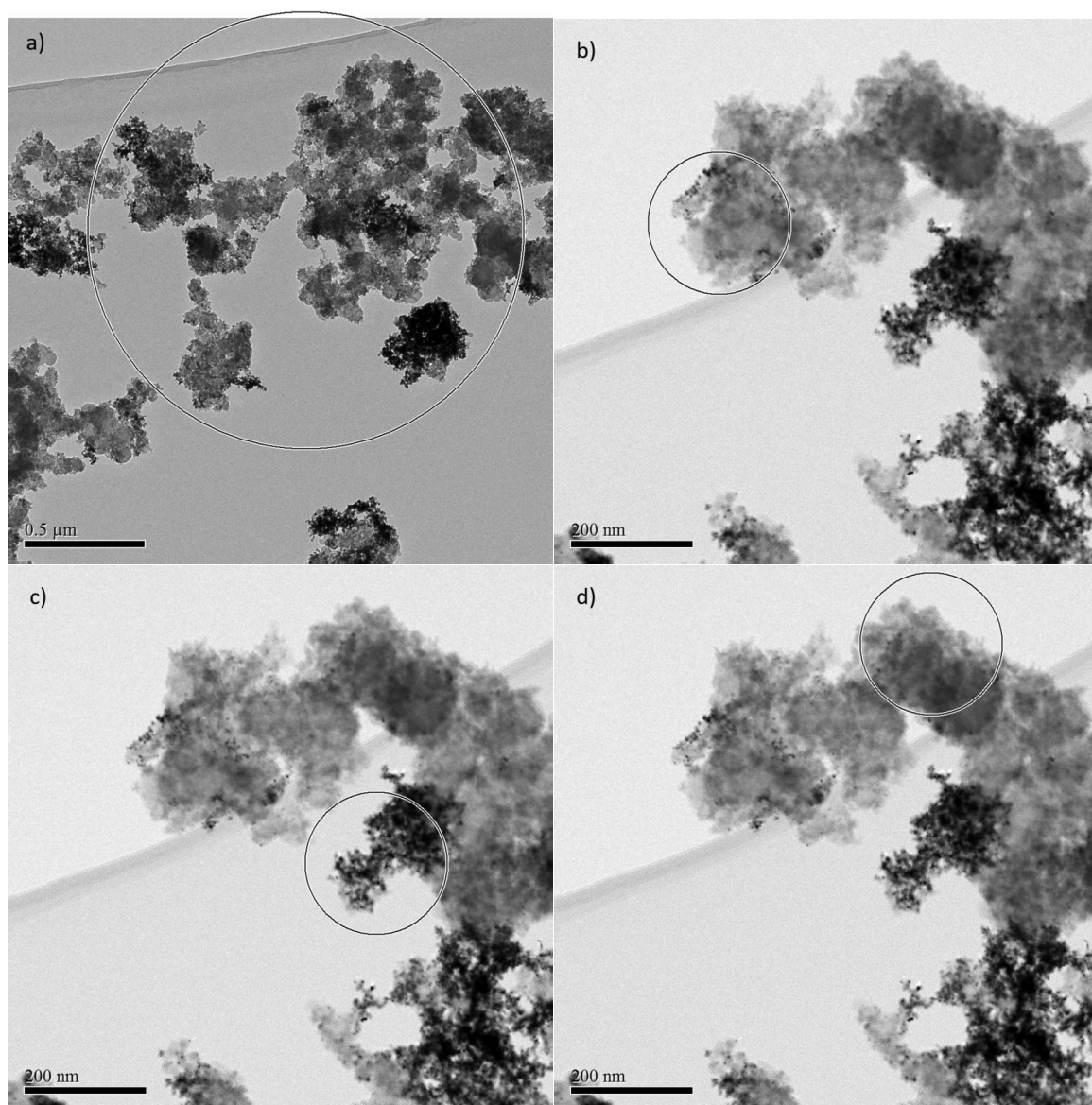


Figure 3.7: TEM of 30%Pt-RuSnO₂/C_{low} (110).

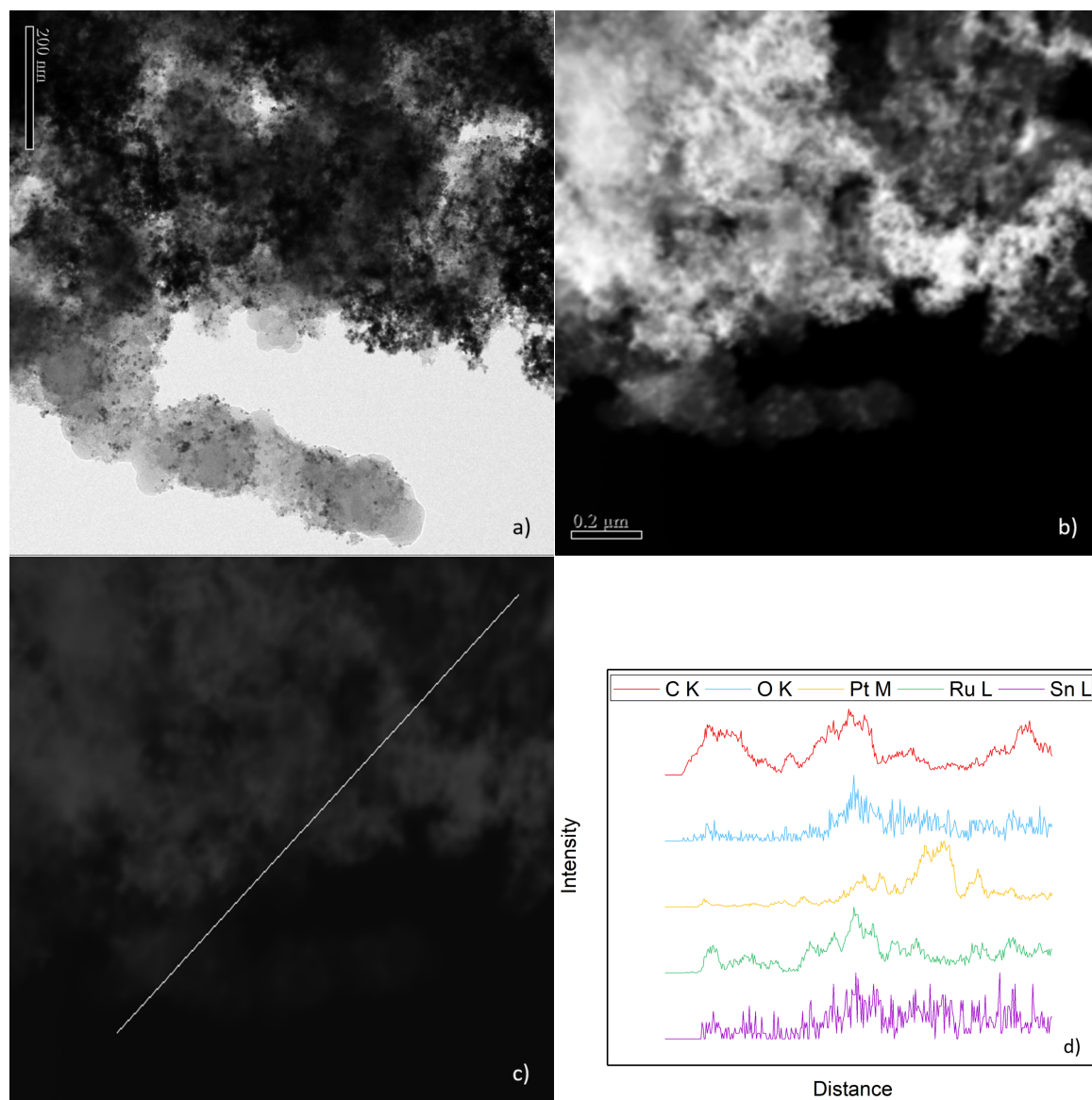


Figure 3.8: TEM image (a), HAADF image (b), line scan analysis (c and d) of 30%Pt-RuSnO₂/C_{low} (110). Note: The EDX spectra in (d) are normalized results and the maximum intensities of all elements are same.

3.6 Conclusions

The preparation of RuSnO_2/C was highly dependant on the pH. KRuO_4 will react with H_2O immediately if the pH is too low and formation of hydrous SnO_2 will not be favored if the pH is too high. Hence, the preparation condition needs further improvements to achieve a slow and quantitative co-deposition of Ru oxide and Sn oxide onto carbon.

A higher amount of RuSnO_2 helped Pt disperse better while a higher amount of Pt deposition caused severe agglomeration. In 30%Pt- $\text{RuSnO}_2/\text{C}_{low}$ (110), Pt was present as nanoparticle while Ru oxide and Sn oxide were amorphous.

Chapter 4

Cyclic Voltammetric Analysis

4.1 Estimation of Electrochemically Active Surface Area

Because fuel cell (FC) tests are time-consuming and require relatively large amounts of catalyst, it was necessary to screen the catalysts to prioritize them. Cyclic voltammetry is a convenient and informative screening method. To better compare the CV results, it is necessary to calculate the electrochemically active surface area (ECSA) of the Pt and normalize the CV results. The determination of ECSA is shown in Equation 4.1 where $210 \mu\text{C cm}^{-2}$ is the charge of full coverage for clean polycrystalline Pt [51].

$$ECSA(\text{cm}^2) = \frac{Q_{H\text{-adsorption}}(\text{C})}{210 (\mu\text{C cm}^{-2})} \quad (4.1)$$

As shown in Figure 4.1 (a), the hydrogen adsorption area and hydrogen desorption area from -0.2 V to ca. 0.1 V (vs. SCE) can be easily observed. The charge for hydrogen adsorption ($Q_{H\text{-adsorption}}$) was used to estimate the ECSA of Pt.

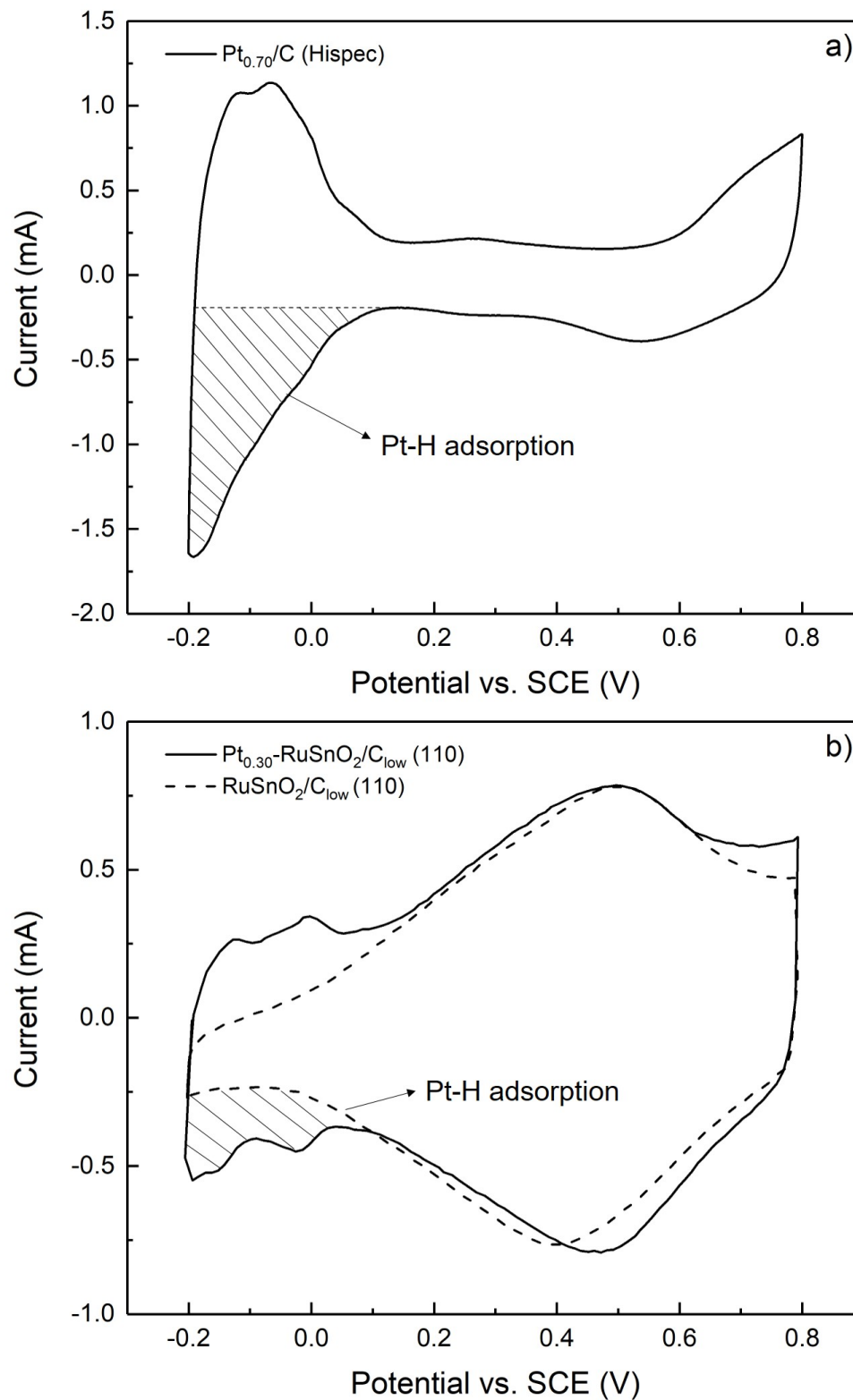


Figure 4.1: Cyclic voltammograms (100 mV/s) of (a) 70%Pt/C (Hispec) and (b) 30%Pt-RuSnO₂/C_{low} (110) and RuSnO₂/C_{low} (110) in 1 M H₂SO₄ (aq). Note: The voltammogram of the RuSnO₂/C_{low} (110) has been scaled to approximately match the Ru-Sn oxide peaks (at ca. 0.5 V) for the 30%Pt-RuSnO₂/C_{low} (110). , Hispec is a trademark, which refers to highly dispersed catalyst.

For Figure 4.1 (b), although the hydrogen adsorption peaks and hydrogen desorption peaks of 30%Pt-RuSnO₂/C_{low} (110) can still be observed, estimation of the charge for hydrogen adsorption was not as easy as for 70%Pt/C because the support contained a large amount of Ru oxide which influenced the charging current. Hence, a scaled CV of its original support (RuSnO₂/C_{low} (110)), shown as the dash line, was used to help estimate the charge for hydrogen adsorption on this catalyst.

For the catalysts whose supports contained higher amounts of Ru oxide and lower amounts of carbon, the estimation of ECSA was done by the procedure shown in Figure 4.1 (b). For other catalysts whose supports contained more C and less Ru oxide, the method shown in Figure 4.1 (a) was used to estimate the ECSA although it will underestimate the ECSA slightly.

4.2 CV of Ethanol at 30%Pt-RuSnO₂/C_{low} (110)

For cyclic voltammetry in 1 M H₂SO₄ (aq) containing 0.1 M ethanol, the scan rate was 10 mV/s instead of 100 mV/s. For application in a FC, the anode catalyst needs to perform well at low potentials, which provides the highest FC potentials. Hence, we mainly focus on the potential range from 0.2 V to 0.4 V (vs. SCE). As can be seen in Figure 4.2, the current started to increase at a very low potential (ca. 0.05 V vs. SCE) when the 30%Pt-RuSnO₂/C_{low} (110) catalyst was used. The current in the forward scan is mainly due to the oxidation of ethanol. After 0.6 V, the current started to decrease. This is due to the formation of an oxide layer that inhibits ethanol adsorption. In the backward scan, the current for ethanol oxidation increased to a peak at ca. 0.5 V when the oxide layer was reduced.

The second forward scan showed lower current than the first one. This suggests that the catalyst may adsorb more ethanol before the experiment than during scan-

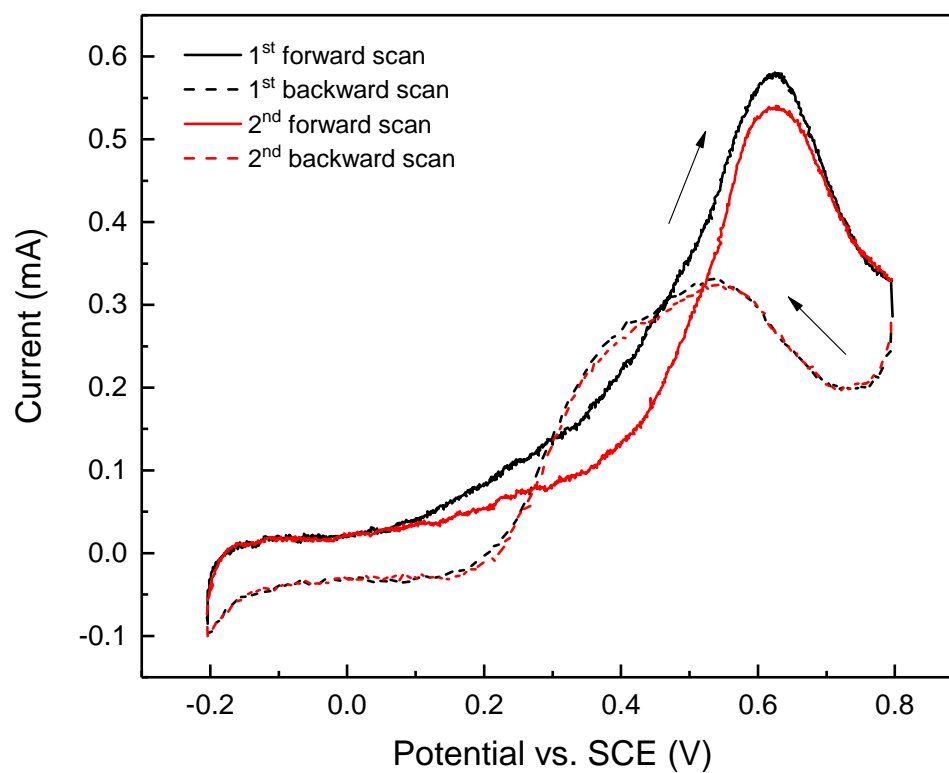


Figure 4.2: Cyclic voltammogram (10 mV/s) of 30%Pt-RuSnO₂/C_{low} (110) in 1 M H₂SO₄ (aq) containing 0.1 M ethanol.

ning. The second backward scan showed almost the same current as the first backward scan which suggests the poisoning in the two forward scans was quite similar. The same behavior was observed for other catalysts, with the second forward current being lower than the first one and the backward currents being almost same.

4.3 Effect of Various Preparation Conditions

To find out the support effect of Ru oxide and Sn oxide, various preparation conditions were used. As discussed in Chapter 3, the reaction time (0.5 h) for preparing RuSnO₂/C (110)* was not enough which led to a lower Ru oxide loading compared to RuSnO₂/C (110). With the same reaction time (24 h), the deposition of Ru oxide went well under various pH conditions. As for the deposition of Sn oxide, the lower the pH used, the more deposition was achieved. Based on the CV results, the effects of Ru oxide and Sn oxide on ethanol oxidation at Pt nanoparticles are discussed here.

As shown in Figure 4.3 (a), 25%Pt-RuSnO₂/C (222) had the same performance as 25%Pt-RuO₂/C (110). Since 25%Pt-RuSnO₂/C (222) had only a small amount of Sn oxide, it behaved like 25%Pt-RuO₂/C (110).

As for the 25%Pt-RuSnO₂/C (000), 25%Pt-RuSnO₂/C (057) and 25%Pt-RuSnO₂/C (110)*, their performances at low potentials were quite similar, although 25%Pt-RuSnO₂/C (000) had the highest percentage of Sn oxide. In addition, despite the fact that 25%Pt-RuSnO₂/C (110) contained a little more Ru oxide than 25%Pt-RuSnO₂/C (110)* and 25%Pt-RuSnO₂/C (057), its performance at low potentials was much better. In Figure 4.3 (b), which shows the second forward scans, 25%Pt-RuSnO₂/C (110) was still the best catalyst, while the others all had much more similar performances. Combined with the XRD and ICP-OES results in Chapter 3, it can be concluded that the addition of Sn oxide caused the catalysts to perform better, but

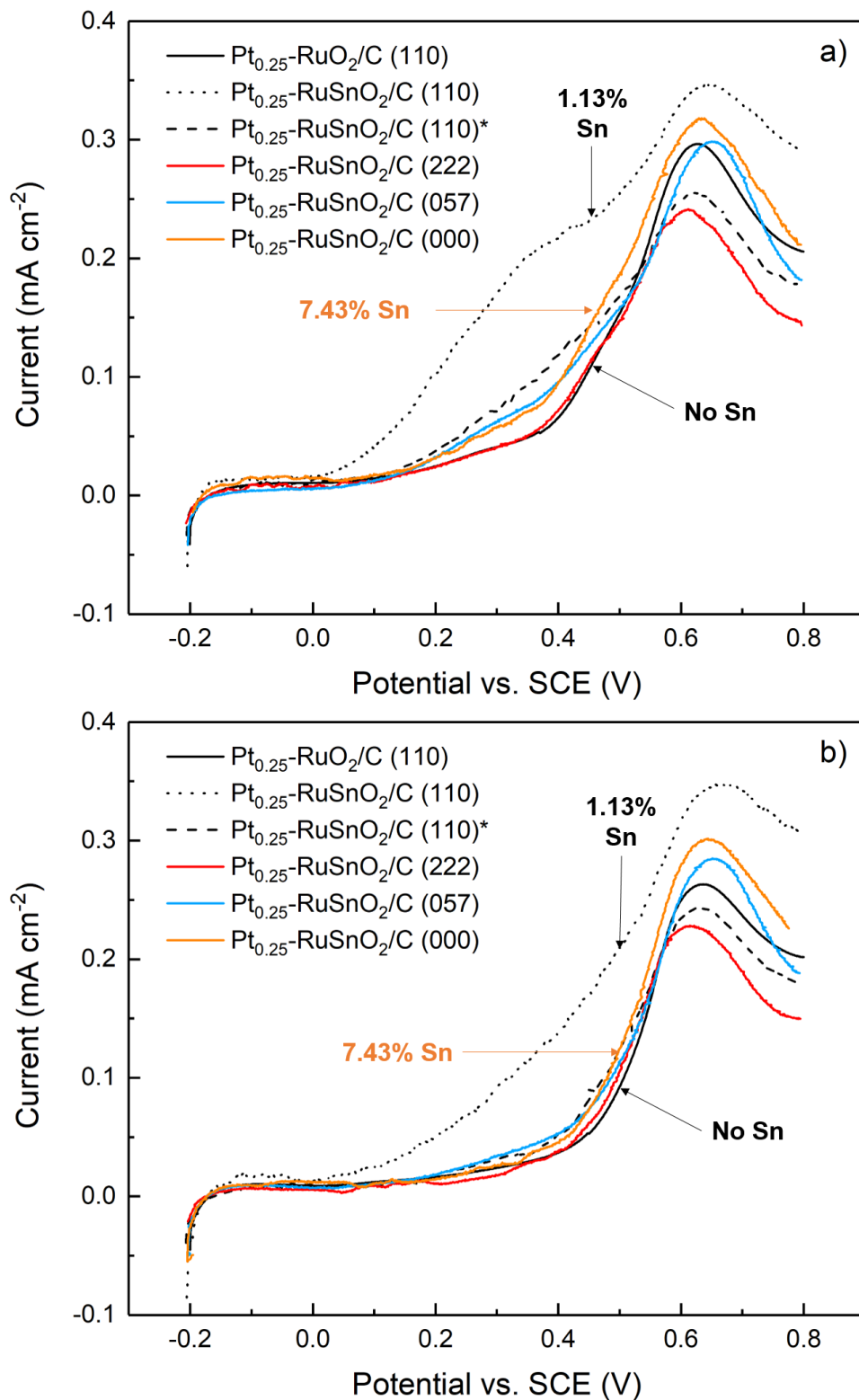


Figure 4.3: Cyclic voltammograms (10 mV/s) of 25%Pt-RuSnO₂/C catalyst in 1 M H₂SO₄ (aq) containing 0.1 M ethanol. (a) First forward scan and (b) second forward scan.

Sn oxide needs to be incorporated into Ru oxide layer to be effective.

4.4 Effect of Heat Treatment and Pt Loading

Here, the effect of heat treatment and Pt loading is discussed. As shown in Figure 4.4, with the Pt content increased, the performance decreased which indicates that low Pt loadings should be used with the RuSnO₂/C (110) support.

As shown in Chapter 2, two kinds of heat treatment were investigated here. One is the heat treatment of the support. For 30%Pt-RuSnO₂/C (110 – 200 °C), its support was heated at 200 °C in air for 12 h and then Pt was deposited onto this support (RuSnO₂/C (110 – 200 °C)). And the other one is the heat treatment of the catalyst. For example, 40%Pt-RuSnO₂/C (110) – 210 °C was heated at 210 °C in air for 12 h but its support was RuSnO₂/C (110) without heat treatment.

Although 30%Pt-RuSnO₂/C (110 – 200 °C) had the highest low-potential current before 0.2 V and highest peak current at ca. 0.6 V (Figure 4.4), its turning point of increasing current was at much higher potential (ca. 0.3 V vs. 0.05 V) than for 30%Pt-RuSnO₂/C (110). As shown in Appendix B.1 and B.2, it is very hard to see the Pt-H desorption peaks at the 30%Pt-RuSnO₂/C (110 – 200 °C) electrode compared with the 30%Pt-RuSnO₂/C (110) electrode and the Pt-H adsorption area at 30%Pt-RuSnO₂/C (110 – 200 °C) electrode was much smaller. Therefore, the ECSA of 30%Pt-RuSnO₂/C (110 – 200 °C) may be underestimated due to the severe influence of the Ru-Sn oxide charging current, which can lead to a higher apparent current density. As for 40%Pt-RuSnO₂/C (110) – 130 °C and 40%Pt-RuSnO₂/C (110) – 210 °C, their performances in the first forward scan between ca. 0.35 V to ca. 0.55 V were better than that of 40%Pt-RuSnO₂/C (110) and their performances in the second forward scan were almost the same.

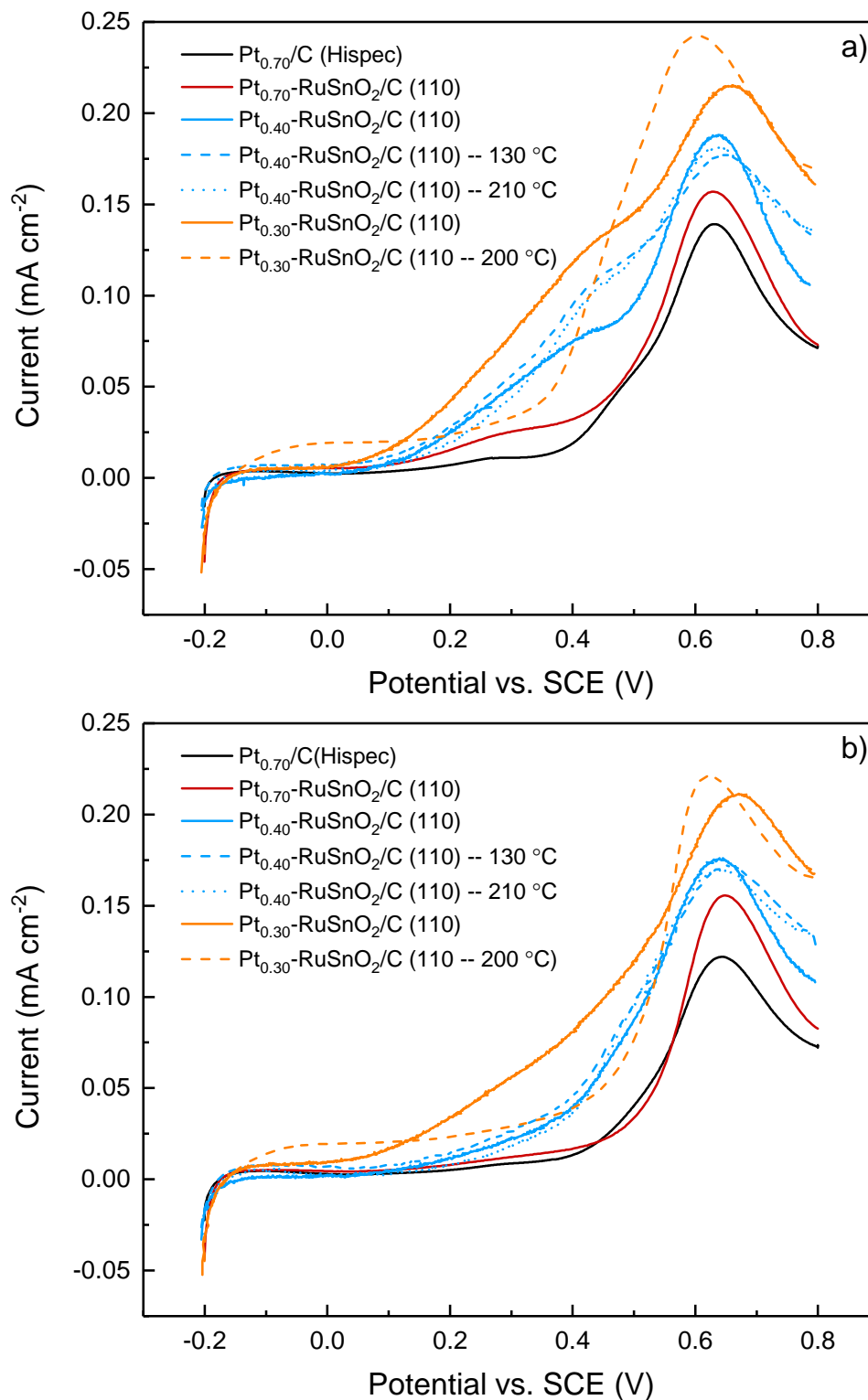


Figure 4.4: Cyclic voltammograms (10 mV/s) of different catalysts in 1 M H₂SO₄ (aq) containing 0.1 M ethanol. (a) First forward scan and (b) second forward scan.

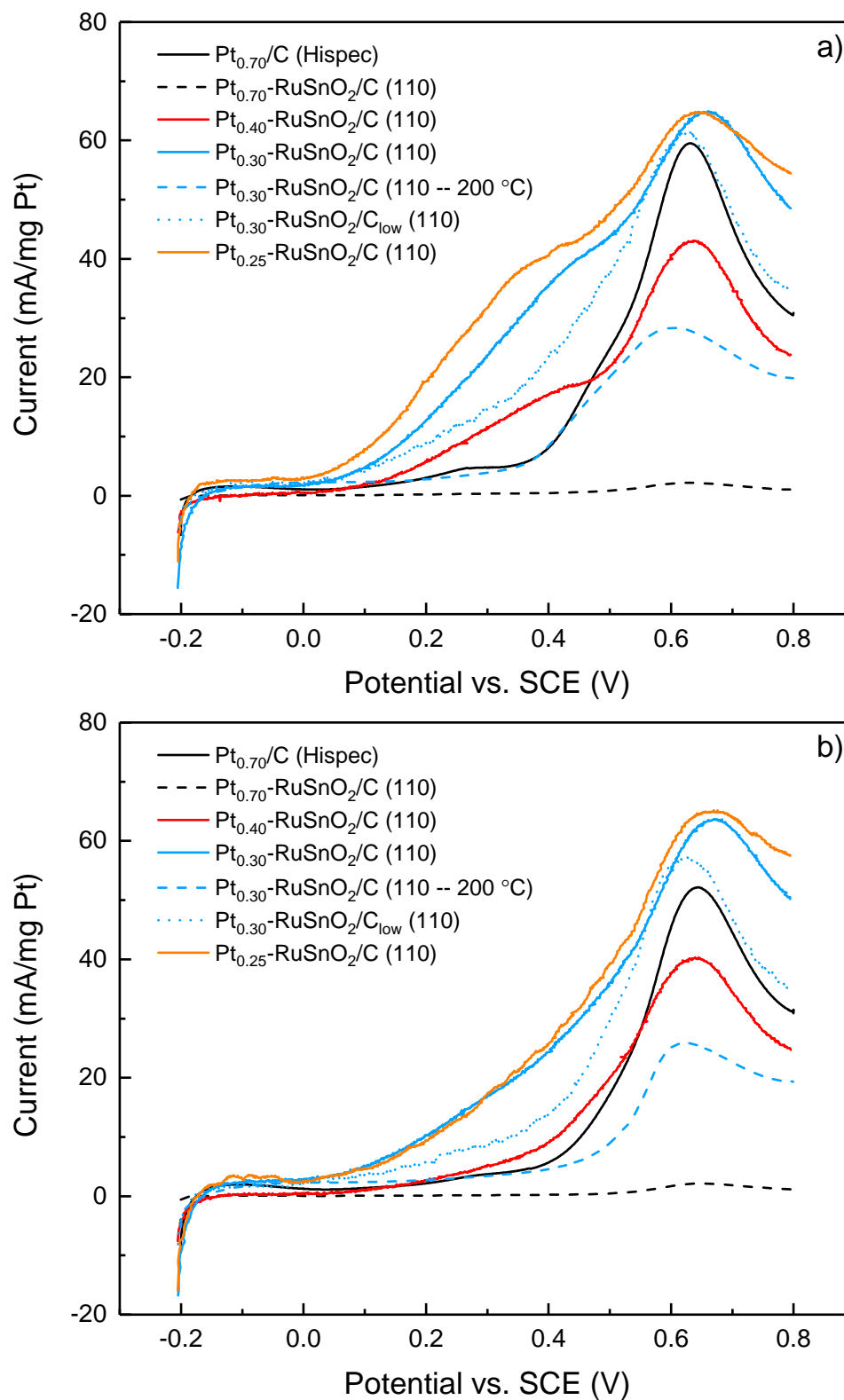


Figure 4.5: Pt utilization: Cyclic voltammograms (10 mV/s) of different catalysts in 1 M H₂SO₄ (aq) containing 0.1 M ethanol. (a) First forward scan and (b) second forward scan.

Based on the catalyst mass used in the ink preparation and nominal Pt percentage, the amount of Pt applied to GC electrodes can be roughly calculated. This current (mA/mg Pt) can give some information about the utilization of Pt. As shown in Figure 4.5, the current for 70%Pt-RuSnO₂/C (110) was really low on this basis, which indicates that the utilization of Pt in this catalyst was small. This phenomenon can be explained by looking at Figure 3.5 (b) which shows a severe agglomeration of the Pt. In Figure 4.5, the current for 30%Pt-RuSnO₂/C (110–200 °C) was much lower than that for 30%Pt-RuSnO₂/C (110), which suggests that the higher current of 30%Pt-RuSnO₂/C (110–200 °C) in Figure 4.4 was very possibly due to the underestimation of ECSA.

Therefore, it can be concluded that the as-prepared RuSnO₂/C (110) support is not suitable for a higher amount of Pt, that heat treatment of the support should be avoided and that heat treatment of the catalysts may have some positive effects.

4.5 Conclusions

The presence of hydrous Ru oxide makes the estimation of ECSA complicated. Except for Pt-RuSnO₂/C_{low} (110), ECSA for other catalysts may have been underestimated which would cause overestimation of the current density (mA cm⁻²). Considering that the main objective here was to observe the shape of the CVs and how well the catalysts performed at lower potentials, this minor inaccuracy is acceptable.

Combined with the XRD and ICP-OES results, it can be concluded that the presence of Sn oxide in the support is necessary to improve performance at low potentials but Sn oxide needs to be incorporated into Ru oxide layer to be effective. Heating of supports and heat treatment of catalysts may be not necessary. RuSnO₂/C may not be suitable for high Pt loadings.

Chapter 5

Ethanol Electrolysis Cell Results

5.1 Introduction

A good anode catalyst for direct ethanol fuel cells, not only needs to be highly active at low potentials, but also should produce as much CO₂ as possible. This is can be explained by the following equations [52]:

$$\varepsilon_{cell} = \varepsilon_t \times \varepsilon_E \times \varepsilon_F \quad (5.1)$$

Where ε_t is the theoretical energy-conversion efficiency (96% at 80 °C), ε_E is the voltage efficiency (see Equation 5.2) and ε_F is the faradic efficiency (see Equation 5.3).

$$\varepsilon_E = \frac{E_{cell}}{E_{rev}} \quad (5.2)$$

E_{cell} is the actual operating cell voltage ($E_{cell} = E_{cathode} - E_{anode} - i \cdot R$), i is the current of the cell and R is the ohmic resistance of the cell. E_{rev} is the reversible cell voltage (ca. 1.14 V).

$$\varepsilon_F = \frac{n_{av}}{n_t} \quad (5.3)$$

n_{av} is the the average number of electrons transferred per molecule of ethanol, which depends on the product distribution. The more complete the ethanol oxidation is, the higher the average number will be. n_t is the number of electrons for the complete oxidation to CO_2 , which is 12.

So if the anode catalyst is highly active even at low potentials, the operating cell voltage will be high and the voltage efficiency will be high. If most of the ethanol is oxidized to CO_2 , a high faradic efficiency will be achieved.

The cyclic voltammetry experiments reported in Chapter 4 were used to examine the catalytic activity towards ethanol oxidation. The catalyst was tested in a three-electrode cell where the electrolyte was stationary. During the CV measurements, the coverage of poisoning intermediates on the catalyst surface was changing. However, in a FC, the catalyst works at a certain potential in a flowing electrolyte where the fuel (ethanol) will be replenished and the products will be discharged constantly, which means the poisoning will be at a steady-state. So it is crucial to examine the catalyst under steady-state conditions. Here, a 9-anode proton exchange membrane electrolysis cell (as shown in Figure 2.1) was used and each potential was held for 3 min for the current measurements.

It is worth noting that the 9-anode cell is good to examine the activity (current) of catalyst towards ethanol oxidation, but not suitable for product analysis since each anode is very small (0.236 cm^2) where only a small amount of ethanol was consumed and also the ethanol oxidation on the catalyst had very limited reaction time. Therefore, a large single-anode (5 cm^2) cell was used for product analysis. Since the experiment in the 5 cm^2 single-anode cell is time-consuming and requires a large amount of catalyst, only the best catalyst ($30\% \text{Pt-RuSnO}_2 / C_{low}$ (110)) was tested.

5.2 Screening of Catalysts in a 9-Anode Cell

To have a stable and controllable ethanol supply, crossover mode (fuel is supplied from the cathode and crosses over through the membrane to the anode) was used, as described by Brueckner et al. [48]. As shown in Figure 5.1, among the 25%Pt series of catalysts, the current at low potentials for 25%Pt-RuSnO₂/C (110) was higher than for the other two catalysts which agrees with the CV results. 30%Pt-RuSnO₂/C_{low} (110) gave the highest current at low potentials (below 0.4 V), hence, it was selected for further testing in the 5 cm² single-anode cell (Section 5.3).

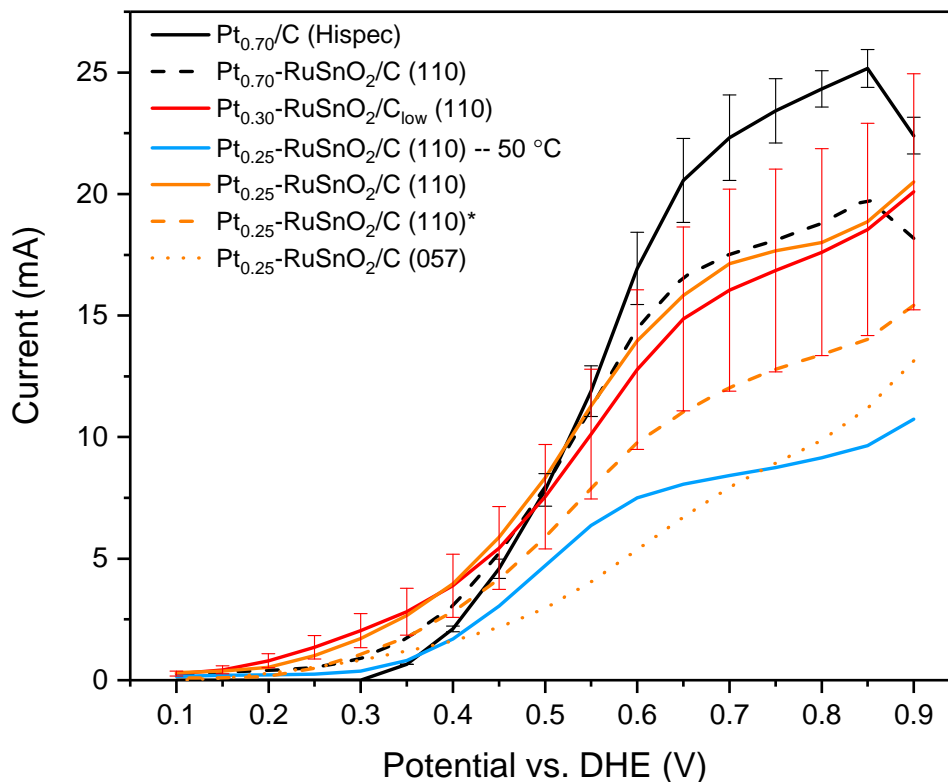


Figure 5.1: Comparison of polarization curves for different anode catalysts (4.0 mg Pt cm⁻²), at 80 °C (except the one labelled 50 °C), in a 9-anode ethanol electrolysis cell operated in a crossover mode (1 M ethanol was passed through the cathode flow field). Representative error bars (standard deviations for 3 electrodes) were shown for two data sets.

When the temperature of the cell was decreased from 80 °C to 50 °C for the 25%Pt-

RuSnO₂/C (110) electrode, the current decreased to about half. This indicates that the temperature is a key parameter for the cell performance. In addition, since the area of each anode was only 0.236 cm², it is difficult to control the loading of the catalyst accurately. To a certain extent, this is reflected by the error bars. Two representative error bars are shown in Figure 5.1. For 70%Pt/C (Hispec), they have random heights, which suggests that the anodes had similar catalyst loadings. As for 30%Pt-RuSnO₂/C_{low} (110), the relative error is almost constant, which suggests that the anodes may have had different loadings of catalyst.

5.3 5 cm² Single-Anode Cell

As one of the best catalysts, 30%Pt-RuSnO₂/C_{low} (110) was tested in the 5 cm² single-anode cell. The steady-state current was measured over a range of potentials and compared with data for the 70%Pt/C (Hispec) catalyst (see Figure 5.2). At low potentials, the performance of 30%Pt-RuSnO₂/C_{low} (110) was much better than that of 70%Pt/C (Hispec). For example, at 0.3 V, the current at the 30%Pt-RuSnO₂/C_{low} (110) anode was three times than at 70%Pt/C (Hispec), although its Pt loading (2.6 mg cm⁻²) was lower than for 70%Pt/C (Hispec) (3.2 mg cm⁻²).

As discussed before, CO₂, acetic acid and acetaldehyde are the main products of ethanol oxidation and a good catalyst should give a high CO₂ yield since CO₂ is the product after complete oxidation. Hence, the faradaic yield of CO₂, f_{CO_2} , is reported in Table 5.1 and it is defined as

$$f_{\text{CO}_2} = \frac{I_{\text{CO}_2}}{I_{\text{total}}} \times 100\% \quad (5.4)$$

where I_{total} is the measured current and I_{CO_2} is the theoretical current required to

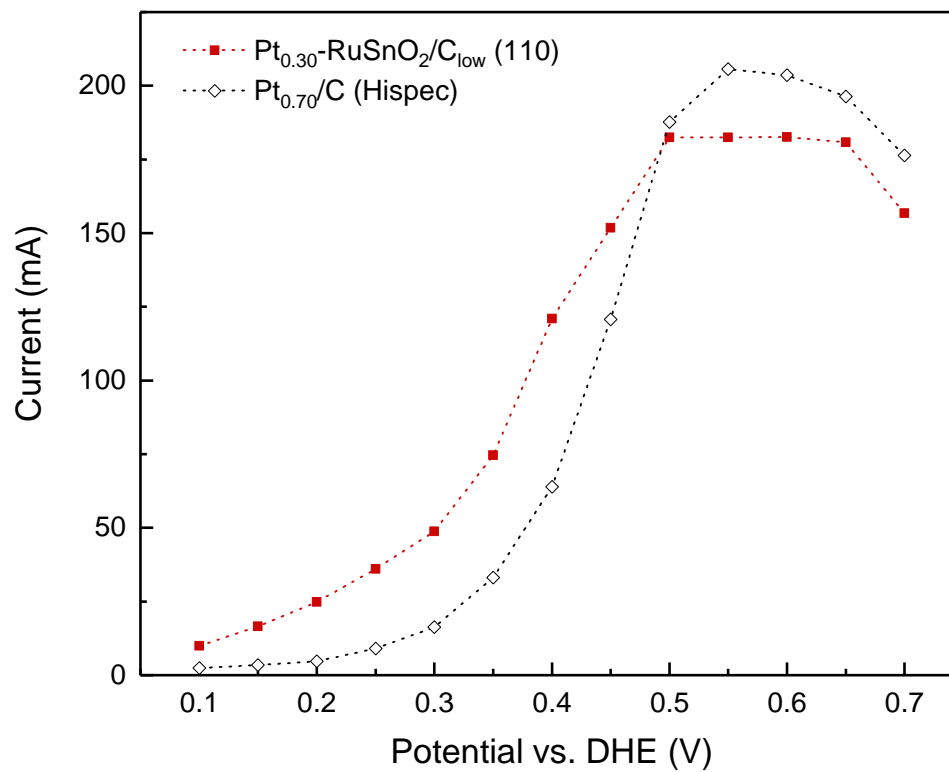


Figure 5.2: Polarization curves for 30%Pt-RuSnO₂/C_{low} (110) (2.6 mg Pt cm⁻²) and 70%Pt/C (Hispec) (3.2 mg Pt cm⁻²) anode catalysts in a 5 cm² single-anode cell, at 80 °C, with 0.1 M ethanol (anode) at 0.5 mL min⁻¹ and N₂ (cathode) at 34 mL min⁻¹. The cathode catalyst was Pt black (4 mg cm⁻²).

form the CO_2 . I_{CO_2} can be calculated by using Equation 5.5.

$$I_{\text{CO}_2} = \frac{c \times 10^{-6} \times V_s}{V_m} \times 6 \times F \quad (5.5)$$

c is the concentration of CO_2 and measured by an NDIR detector which gives a value in parts per million volume. V_s is the volume flow rate (L s^{-1}) of the carrying gas (N_2), V_m is the molar volume (24.2 L mol^{-1} at $80 \text{ }^\circ\text{C}$), 6 is a conversion factor (6 units of electrons are transferred when 1 unit of CO_2 is produced) and F refers to the Faraday constant (96485 C mol^{-1}).

By comparing the results shown in Table 5.1, it can be seen that the faradaic yield of CO_2 for 70%Pt/C (Hispec) was much higher than for 30%Pt-RuSnO₂/C_{low} (110). However, the current for 70%Pt/C (Hispec) was much lower than for 30%Pt-RuSnO₂/C_{low} (110) at low potentials (under 0.40 V), which indicates that more ethanol was consumed in the EEC with 30%Pt-RuSnO₂/C_{low} (110) under those conditions although less ethanol was oxidized to CO_2 . Therefore, it can be concluded that 30%Pt-RuSnO₂/C_{low} (110) is much more active towards ethanol oxidation at low potentials than 70%Pt/C (Hispec), but the complete oxidation of ethanol is more favored in the 70%Pt/C (Hispec) anode.

Table 5.1: Current and faradic yields of CO_2 for ethanol oxidation (0.100 M at 0.2 mL min^{-1}) at different anodes in a 5 cm^2 cell at $80 \text{ }^\circ\text{C}$.

Potential vs. DHE (V)	0.20	0.25	0.30	0.35	0.40	0.45	0.50	0.60	0.70
70%Pt/C (Hispec)									
I_{total} (mA)	4.5	-	15.5	-	55.5	-	128.6	135.3	-
$[\text{CO}_2]$ (ppm)	347	-	825	-	2943	-	7899	7728	-
f_{CO_2} (%)	97.4	-	67.0	-	66.6	-	77.1	71.4	-
30%Pt-RuSnO ₂ /C _{low} (110)									
I_{total} (mA)	24.0	33.6	49.6	69.3	90.7	98.9	-	108.8	97.4
$[\text{CO}_2]$ (ppm)	252	404	629	862	1515	2342	-	3460	2239
f_{CO_2} (%)	14.2	16.3	17.2	16.9	22.7	32.1	-	43.1	31.2

Although faradaic yield of CO_2 can provide some mechanistic information, a complete analysis of products is required to calculate the faradaic efficiency of the cell and investigate the mechanism. Here, the product analysis was done by using a similar method to Altarawneh et al. [13]. The exhaust from both sides of the cell was collected in a trap cooled with an ice-dry ice mixed bath for quantitative product collection (acetaldehyde is very volatile).

Figure 5.3 shows an NMR spectrum, in which the peaks of ethanol, acetic acid and acetaldehyde can be observed. The detailed results are shown in Table 5.2. With the help of a known concentration of fumaric acid (internal standard), the concentrations of products and the residual ethanol can be easily obtained. Considering the influence of background correction, the H1 peak instead of the H5 peak was used to determine the concentration of ethanol and the H4 peak instead of the H7 peak was used to determine the concentration of acetaldehyde. Because a dimer of acetaldehyde is formed under these conditions [53], the actual concentration of acetaldehyde consists of the concentration of acetaldehyde and the concentration of its dimer.

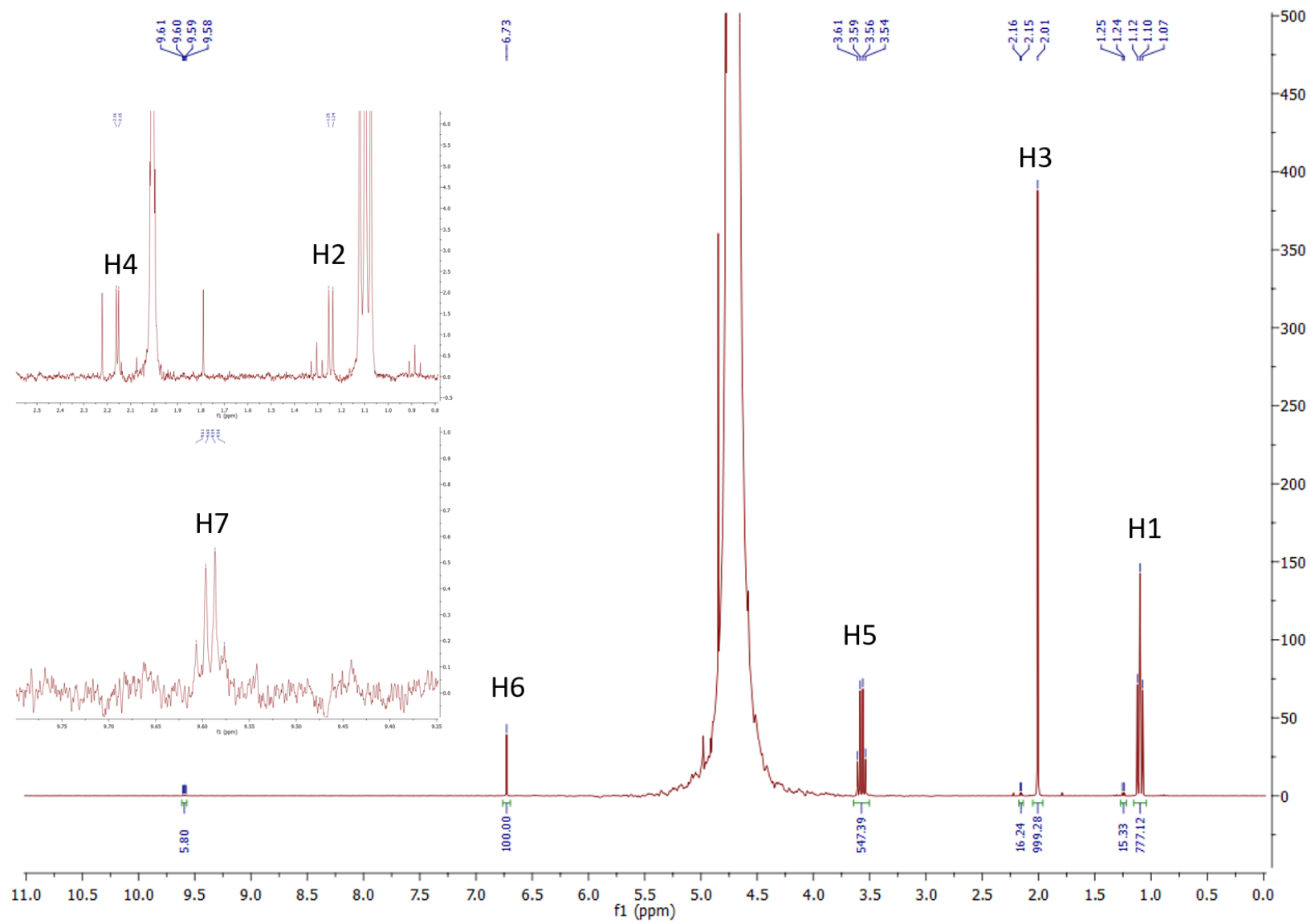


Figure 5.3: $^1\text{H-NMR}$ (300 MHz) spectrum of a mixture of fumaric acid solution (D_2O) and the exhaust solution from EEC operated with 0.1 M ethanol at 0.45 V and 80 $^\circ\text{C}$. Anode catalyst: 30%Pt-RuSnO₂/C_{low} (110).

Table 5.2: Peak assignment for Figure 5.3 with corresponding components and concentrations.

Peak Name	Component	Group	$\delta(ppm)$	Integral	Concentration (mM)
H1	Ethanol	CH ₃	1.10	777	38.9
H2	Dimer(AAL)	CH ₃	1.24	15.3	0.77
H3	AA	CH ₃	2.01	999	50.0
H4	AAL	CH ₃	2.16	16.2	0.81
H5	Ethanol	CH ₂	3.57	547	41.1
H6	Fumaric Acid	COOH	6.73	100	6.00
H7	AAL	CHO	9.59	5.80	0.87

AAL is acetaldehyde and AA is acetic acid.

The product distribution results of the 30%Pt-RuSnO₂/C_{low} (110) anode are shown in Table 5.3, together with the data for a 70%Pt/C (Hispec) anode from another experiment and for a 75%PtRu/C anode from ref. [13]. At 0.45 V, the current, the yield of CO₂ and faradaic efficiency at the 30%Pt/S_{LC} anode were all intermediate between the values at the 70%Pt/C anode and at the 75%PtRu/C anode. Thus, it can be concluded that the increased electrochemical performance of 30%Pt/S_{LC} over 70%Pt/C comes at a lower trade-off in faradaic efficiency than for 70%PtRu/C. It is also worthy to note that the 30%Pt/S_{LC} anode produced much less acetaldehyde than the 70%Pt/C anode and so would decrease harmful emissions from DEFCs [54].

Table 5.3: Currents, chemical yields of products, stoichiometries, and faradaic efficiencies for ethanol oxidation (0.1 M at 0.2 mL min⁻¹) at 70%Pt/C, 30%Pt/S_{LC}, and 75%PtRu/C anodes in a 5 cm² PEM electrolysis cell at 80 °C. (70%Pt/C refers to 70%Pt/C (Hispec), 30%Pt/S_{LC} refers to 30%Pt-RuSnO₂/C_{low} (110), the results of 75%PtRu/C is from Ref. [13]).

Potential vs. DHE (V)	Anode catalyst	Current (mA)	CO ₂ (%)	AA (%)	AAL (%)	n _{av}	ϵ_f (%)
0.45	70%Pt/C	78	37.6	48.2	14.1	6.7	56
0.45	30%Pt/S _{LC}	95	13.5	82.5	2.9	5.3	44
0.45	75%PtRu/C	107	7.0	84.1	8.9	4.5	38
0.50	70%Pt/C	116	50.2	46.4	3.5	7.9	66
0.50	30%Pt/S _{LC}	110	15.6	84.7	1.7	5.0	42
0.50	75%PtRu/C	117	6.9	92.4	0.8	4.5	38

5.4 Conclusions

The 9-anode cell is useful for screening catalysts for more detailed evaluation in the 5 cm² cell. Polarization curves at low potentials agreed well with the CV results. As for the 5 cm² cell, it is very useful to evaluate the catalyst. By analyzing the polarization curves, faradiac CO₂ yield results and chemical yield results, it can be concluded that the reason for the enhanced performance of 30%Pt-RuSnO₂/C_{low} (110) at low potentials is that 30%Pt-RuSnO₂/C_{low} (110) can consume more ethanol than 70%Pt/C (Hispec) and produce more acetic acid and less acetaldehyde, although 70%Pt/C (Hispec) can produce a high amount of CO₂.

Chapter 6

Summary and Future Work

6.1 Summary

New anode catalysts for direct ethanol fuel cells were developed, which improved catalytic activity towards ethanol oxidation at low potentials and retained relatively high faradaic efficiency. The new anode catalysts consisted of Pt, Ru oxide, Sn oxide and carbon, where carbon black modified with Ru-Sn mixed oxides was used as supports for Pt nanoparticles. The Ru-Sn mixed oxides were mainly amorphous and Pt was present as nanoparticle confirmed by XRD and TEM. TGA was used to estimate the loadings of Ru-Sn oxides and Pt in the supports and catalysts. The deposition of Pt went very well, while the co-deposition of Ru-Sn oxides onto C was highly dependent on the concentration of KOH added. Elemental analysis results from ICP-OES showed that more Sn was deposited when less basic conditions were used. The morphology of the catalyst and element distributions on the surface were investigated by SEM-EDX. Severe agglomeration was observed when a high Pt loading was used. Individual Pt nanoparticles were observed by TEM.

The catalytic activity was first examined by CV analysis at room temperature,

which was very quick and convenient. The prepared catalysts (Pt-RuSnO₂/C) showed higher ethanol oxidation activity at low potentials over the commercial Pt/C catalyst. Then, a nine-anode PEM electrolysis cell was used to further screen the catalysts. The experiments were operated in a crossover mode at 80 °C and had good agreement with the CV results. The best Pt-RuSnO₂/C catalyst (30%Pt-RuSnO₂/C_{low} (110)) was selected for further analysis in a 5 cm² single-anode PEM electrolysis cell. Compared with the commercial Pt/C catalyst, the best Pt-RuSnO₂/C catalyst showed much better low-potential activity. The CO₂ yield and faradaic efficiency for the best Pt-RuSnO₂/C catalyst were both intermediate between the values for Pt/C and PtRu/C. Therefore, the increased low-potential activity of the best Pt-RuSnO₂/C catalyst over Pt/C comes at a lower compromise in faradaic efficiency than for PtRu/C. In addition, the best Pt-RuSnO₂/C catalyst showed a much lower acetaldehyde yield than the commercial Pt/C catalyst, which means the use of the catalyst could decrease the harmful emissions in DEFC. Overall, it can be concluded that Pt-RuSnO₂/C catalysts are better than both Pt/C and PtRu/C for use in DEFCs and EECs.

6.2 Future Work

Nowadays, commercial direct methanol fuel cells are already available. As for DFFCs, although ethanol has lower toxicity and higher energy density than methonal, they are not commercial available yet because of low efficiencies. The good thing about DEFCs is that the system of DEFCs can be very similar to commercial DMFCs. Hence, it is crucial to develop high performance catalysts for DEFCs.

To be useful in DEFCs and EECs, the faradaic efficiency of the Pt-RuSnO₂/C catalyst needs to be further improved. First, the composition and synthetic method of the RuSnO₂/C support should be optimized. Second, various Pt deposition meth-

ods can be tried to avoid high agglomeration and obtain more active nanoparticles. Last but not the least, instead of Pt nanoparticles, Pt alloys, which have high CO₂ selectivity towards ethanol oxidation, should be considered. In particular, alloying Pt with Rh [55] and/or Ni [56] is expected to increase the CO₂ yield.

Appendix A

SEM-EDX

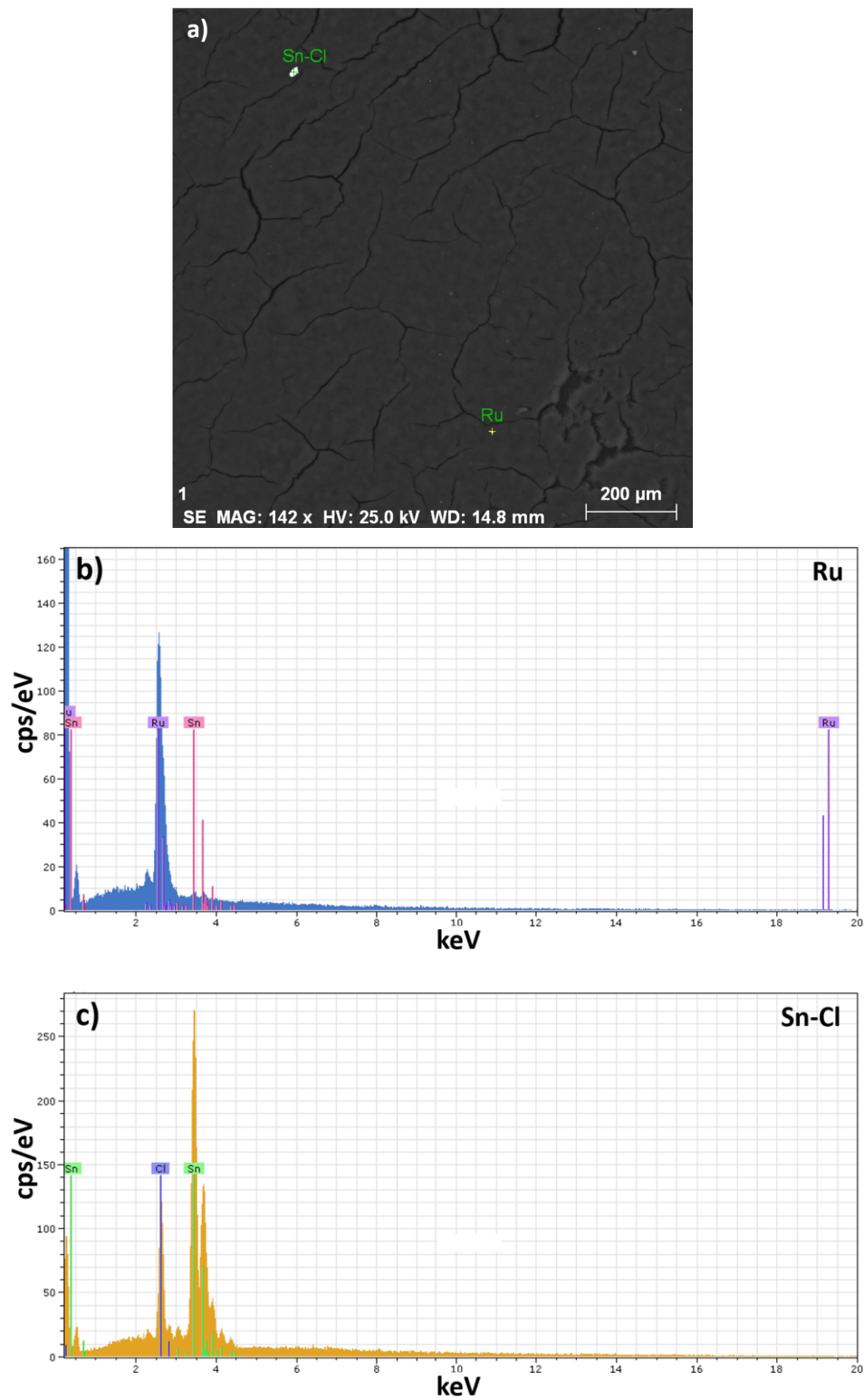


Figure A.1: SEM image (a) and EDX spectra (b and c) for the ICP-OES digestion residue of 30%Pt-RuSnO₂/C_{low} (110)

Appendix B

Cyclic voltammograms

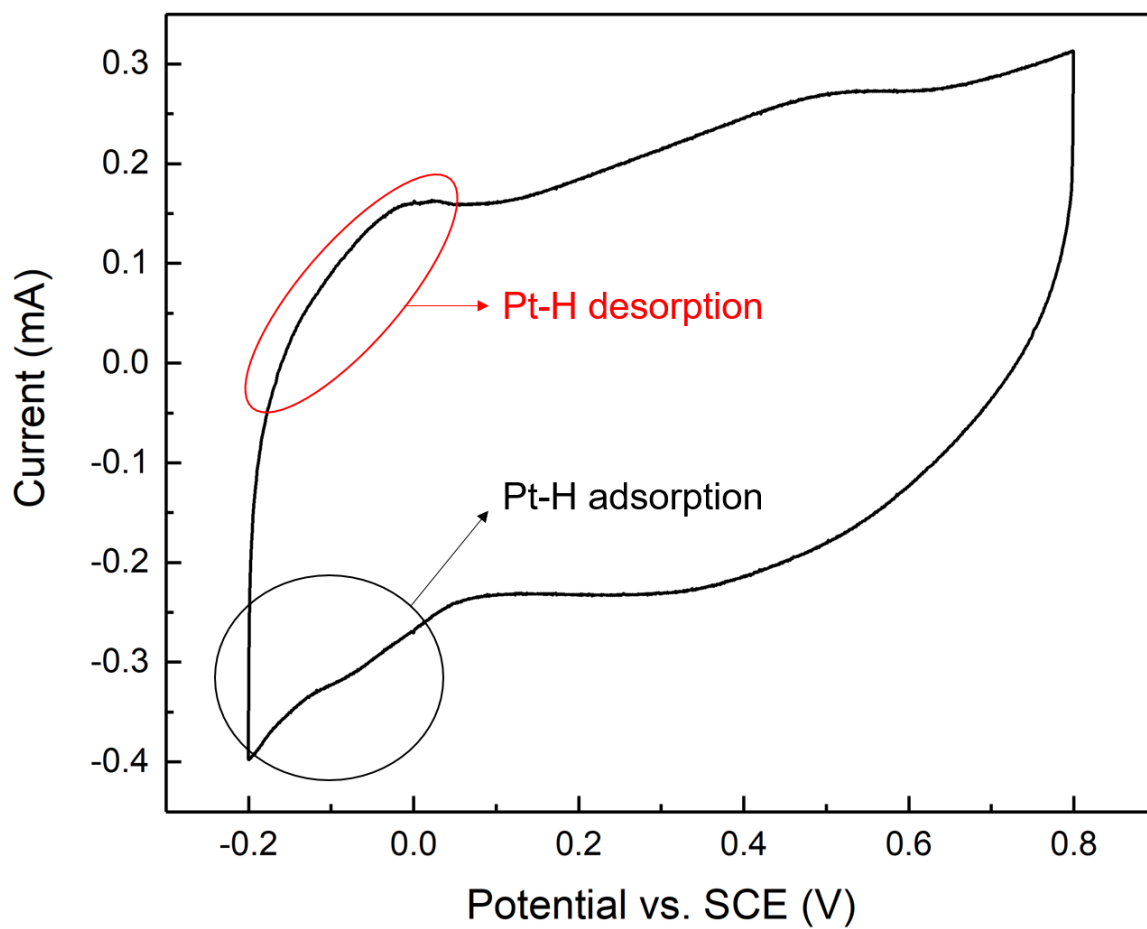


Figure B.1: Cyclic voltammograms (100 mV/s) of 30%Pt-RuSnO₂/C (110–200°C) in 1 M H₂SO₄ (aq).

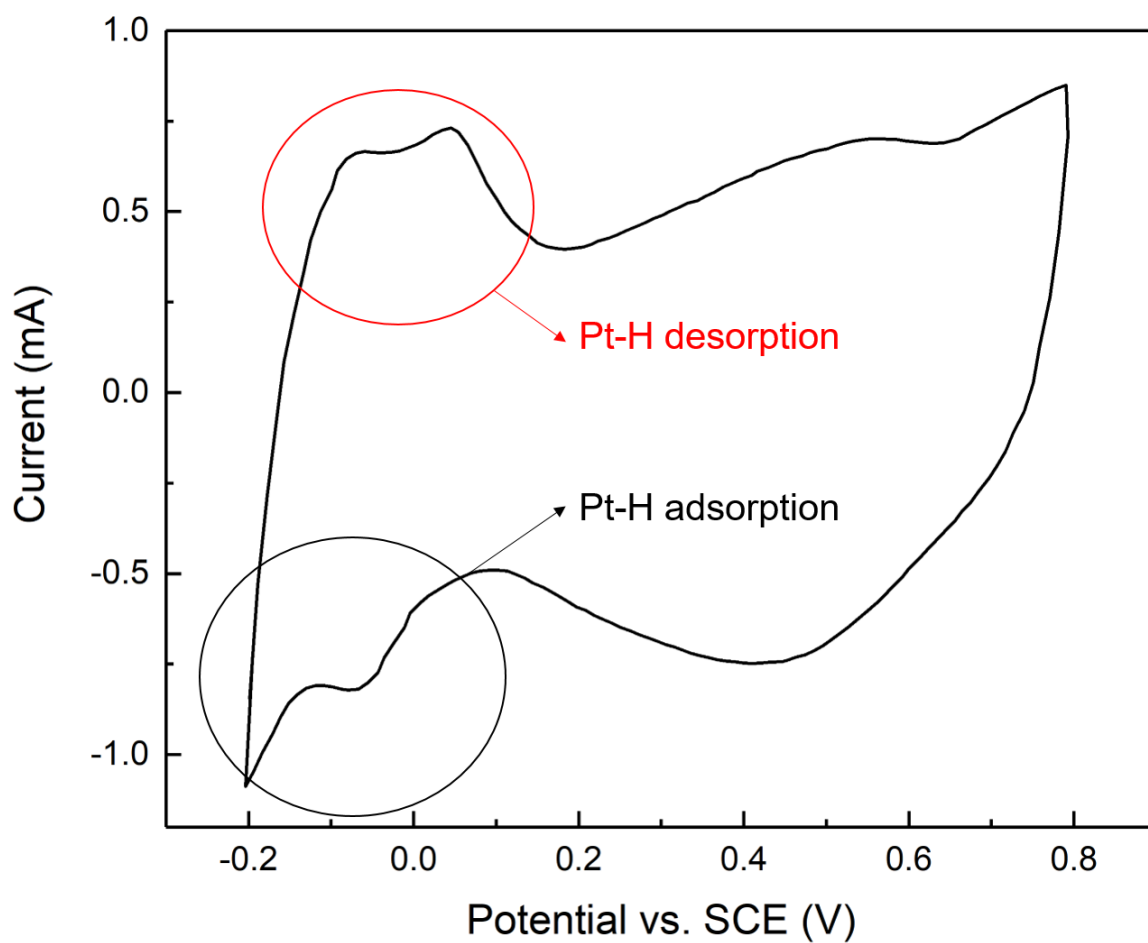


Figure B.2: Cyclic voltammograms (100 mV/s) of 30%Pt-RuSnO₂/C (110) in 1 M H₂SO₄ (aq).

Appendix C

EDX spectra from TEM

experiments and TEM image

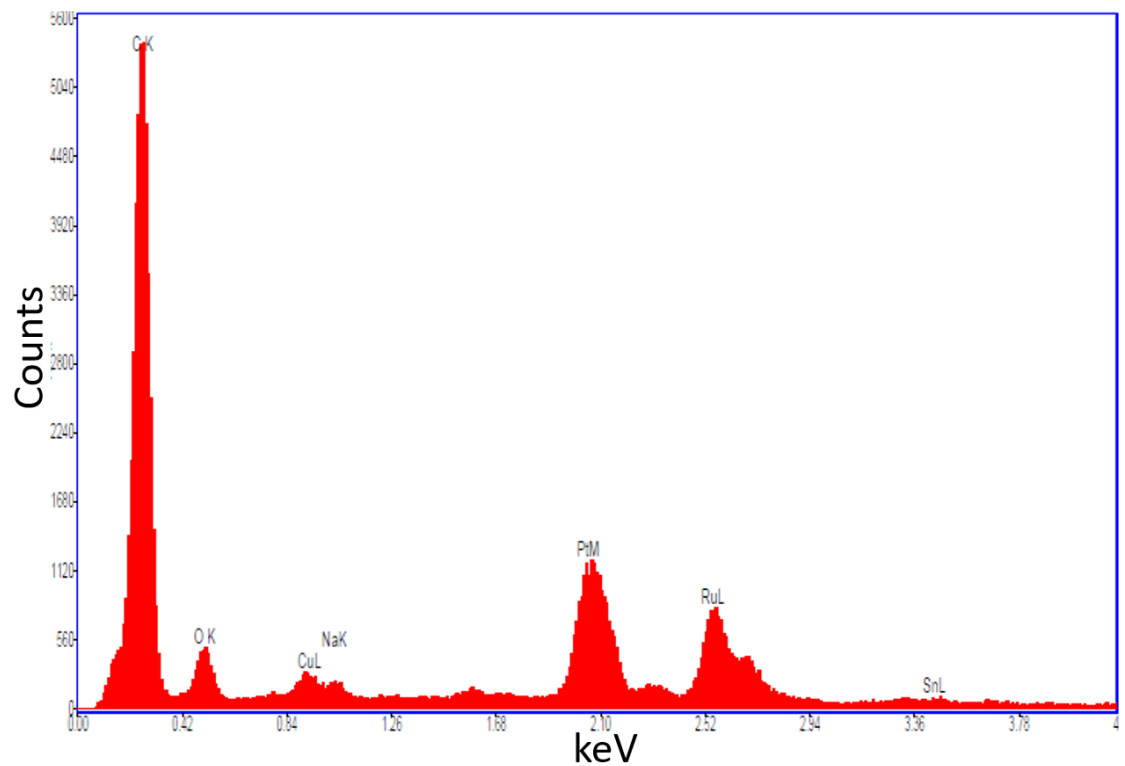


Figure C.1: EDX spectrum of circled area in Figure 3.7(a).

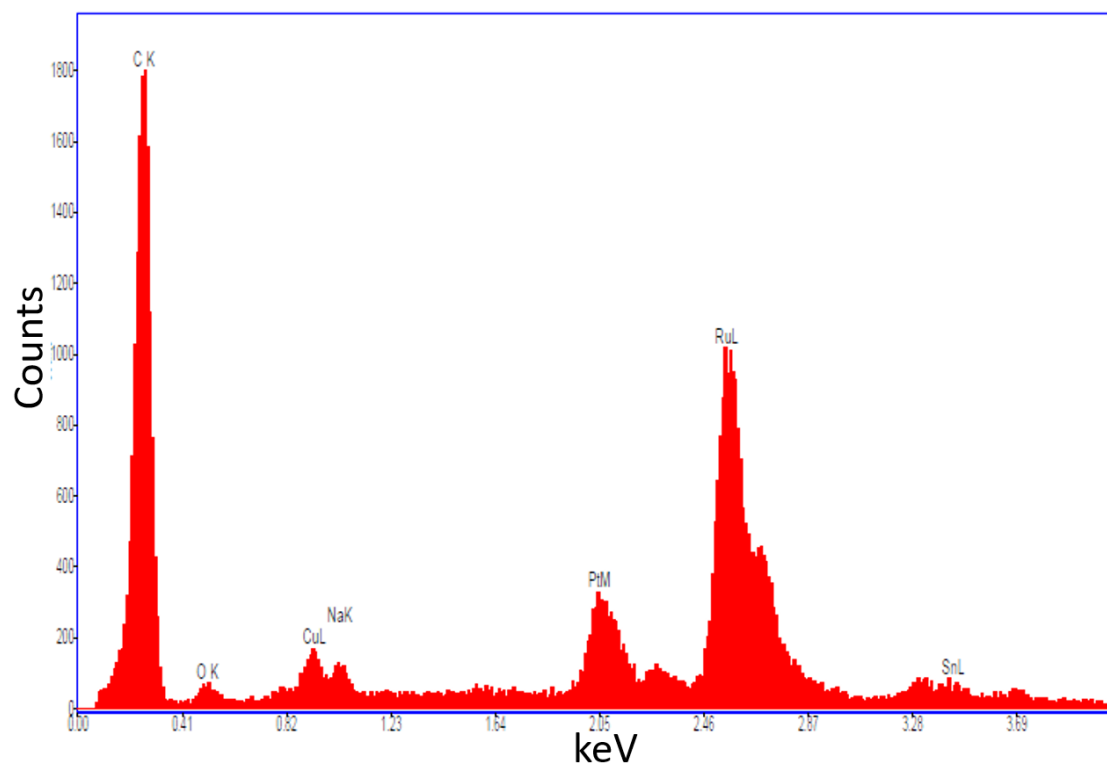


Figure C.2: EDX spectrum of circled area in Figure 3.7(b).

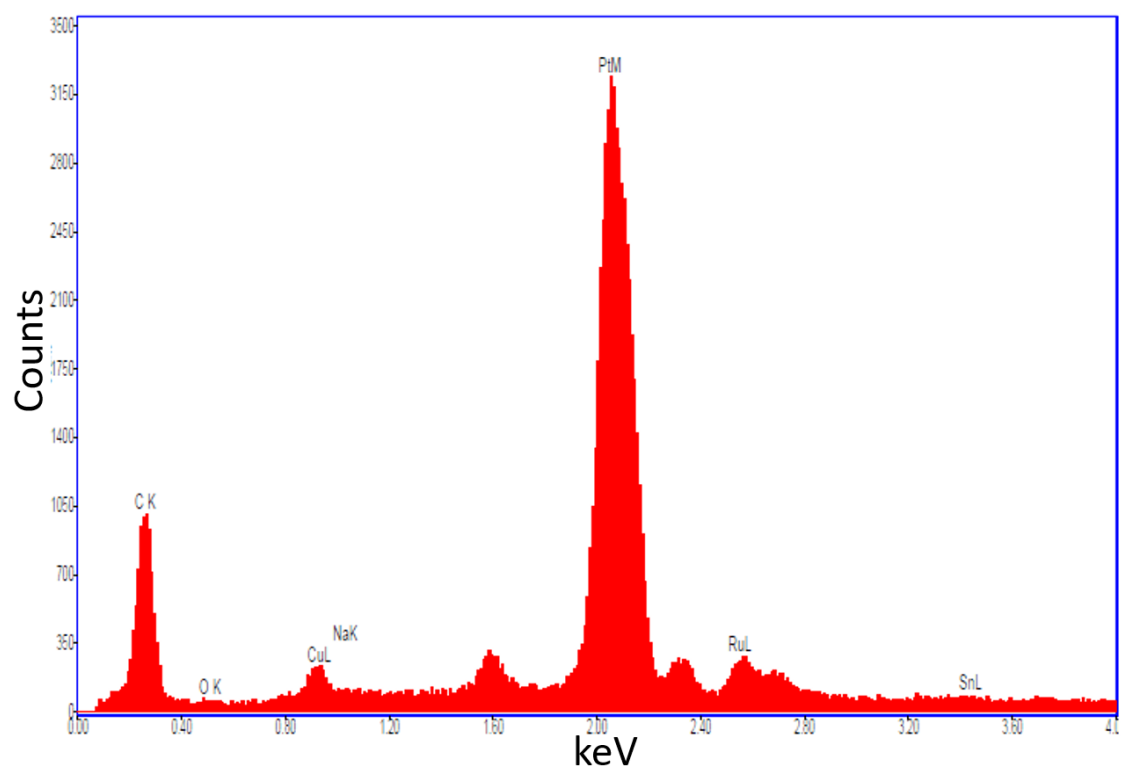


Figure C.3: EDX spectrum of circled area in Figure 3.7(c).

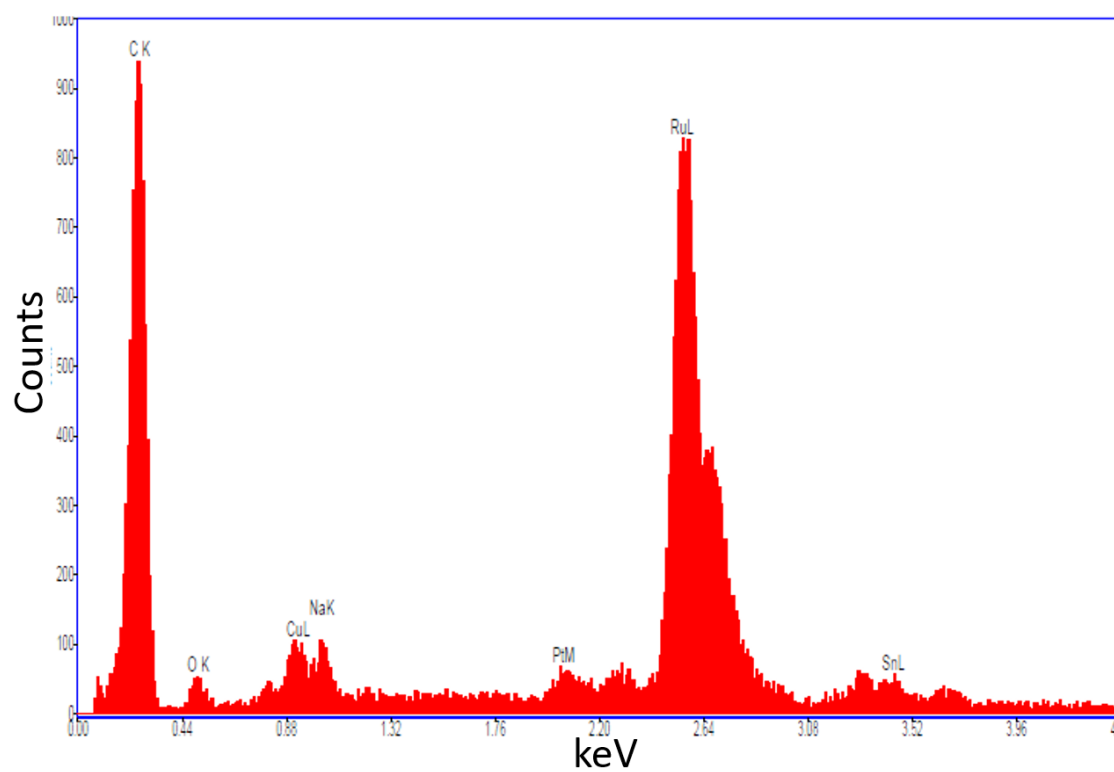


Figure C.4: EDX spectrum of circled area in Figure 3.7(d).

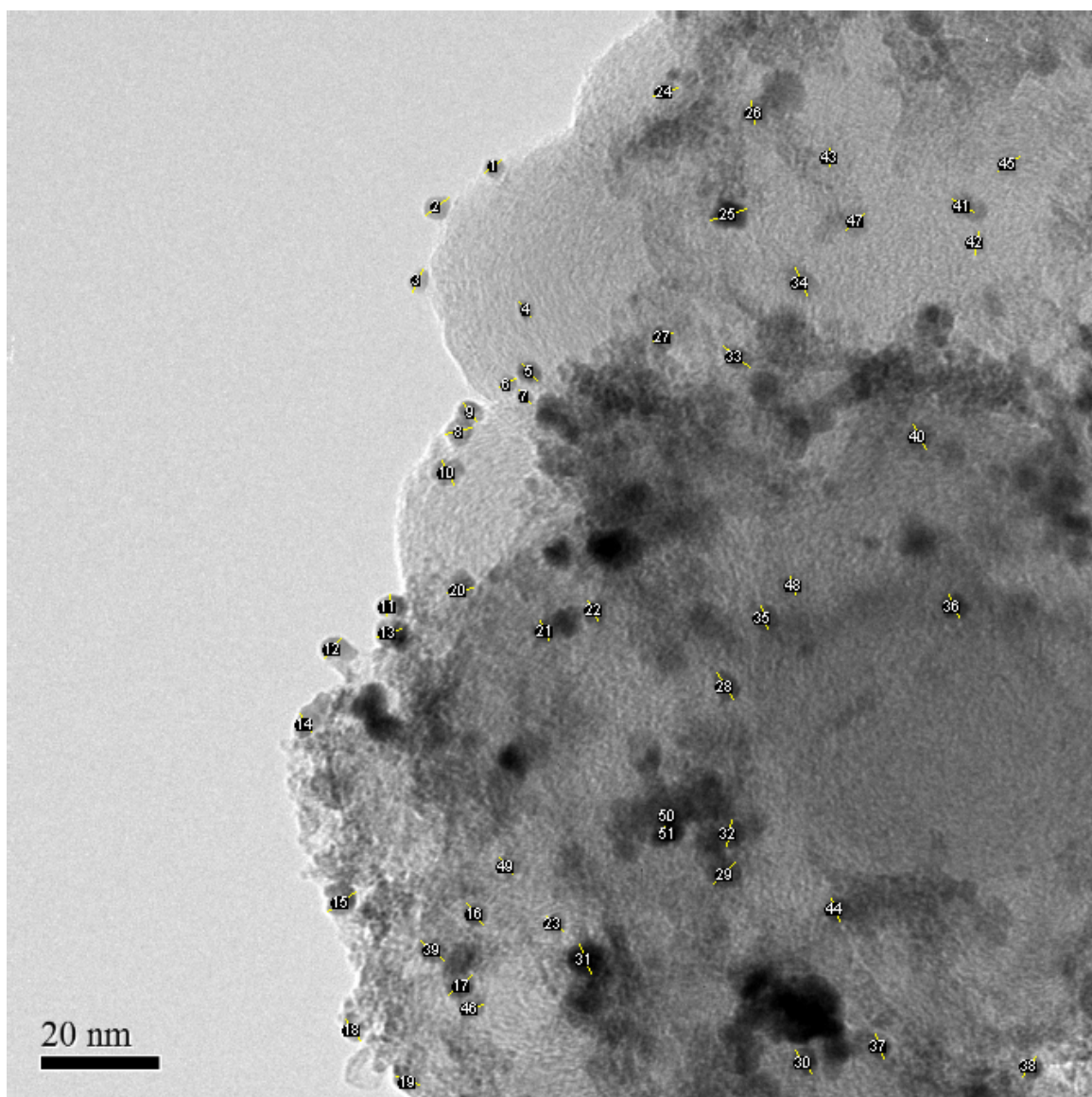


Figure C.5: TEM of 30%Pt-RuSnO₂/C_{low} (110) used for particle size calculation.

Bibliography

- [1] H.R. Corti and E.R. Gonzalez, editors. *Direct alcohol fuel cells*. Springer, 2014.
- [2] K.V. Kordesch and G.R. Simader. Environmental impact of fuel cell technology. *Chemical Reviews*, 95(1):191–207, 1995.
- [3] R. Borup, J. Meyers, B. Pivovar, Y.S. Kim, R. Mukundan, N. Garland, D. Myers, M. Wilson, F. Garzon, D. Wood, P. Zelenay, K. More, K. Stroh, T. Zawodzinski, J. Boncella, J.E. McGrath, M. Inaba, K. Miyatake, M. Hori, K. Ota, Z. Ogumi, S. Miyata, A. Nishikata, Z. Siroma, Y. Uchimoto, K. Yasuda, K.I. Kimijima, and N. Iwashita. Scientific aspects of polymer electrolyte fuel cell durability and degradation. *Chemical Reviews*, 107(10):3904–3951, 2007.
- [4] M.A.F. Akhairi and S.K. Kamarudin. Catalysts in direct ethanol fuel cell (DEFC): An overview. *International Journal of Hydrogen Energy*, 41(7):4214–4228, 2016.
- [5] B.C. Ong, S.K. Kamarudin, and S. Basri. Direct liquid fuel cells: A review. *International Journal of Hydrogen Energy*, 42(15):10142–10157, 2017.
- [6] J. Flórez-Montaño, G. García, O. Guillén-Villafuerte, J.L. Rodríguez, G.A. Planes, and E. Pastor. Mechanism of ethanol electrooxidation on mesoporous Pt electrode in acidic medium studied by a novel electrochemical mass spectrometry set-up. *Electrochimica Acta*, 209:121–131, 2016.

- [7] G.A. Camara and T. Iwasita. Parallel pathways of ethanol oxidation: The effect of ethanol concentration. *Journal of Electroanalytical Chemistry*, 578(2):315–321, 2005.
- [8] Y. Wang, S. Zou, and W. Cai. Recent advances on electro-oxidation of ethanol on Pt- and Pd-Based catalysts: From reaction mechanisms to catalytic materials. *Catalysts*, 5(3):1507–1534, 2015.
- [9] C. Busó-Rogero, S. Brimaud, J. Solla-Gullon, F.J. Vidal-Iglesias, E. Herrero, R.J. Behm, and J.M. Feliu. Ethanol oxidation on shape-controlled platinum nanoparticles at different pHs: A combined in situ IR spectroscopy and online mass spectrometry study. *Journal of Electroanalytical Chemistry*, 763:116–124, 2016.
- [10] F. Vigier, C. Coutanceau, F. Hahn, E.M. Belgsir, and C. Lamy. On the mechanism of ethanol electro-oxidation on Pt and PtSn catalysts: Electrochemical and in situ IR reflectance spectroscopy studies. *Journal of Electroanalytical Chemistry*, 563(1):81–89, 2004.
- [11] A. Bach Delpuch, F. Maillard, M. Chatenet, P. Soudant, and C. Cremers. Ethanol oxidation reaction (EOR) investigation on Pt/C, Rh/C, and Pt-based bi- and tri-metallic electrocatalysts: A DEMS and in situ FTIR study. *Applied Catalysis B: Environmental*, 181:672–680, 2016.
- [12] S. Rousseau, C. Coutanceau, C. Lamy, and J.M. Léger. Direct ethanol fuel cell (DEFC): Electrical performances and reaction products distribution under operating conditions with different platinum-based anodes. *Journal of Power Sources*, 158(1):18–24, 2006.

- [13] R.M. Altarawneh and P.G. Pickup. Product distributions and efficiencies for ethanol oxidation in a proton exchange membrane electrolysis Cell. *Journal of The Electrochemical Society*, 164(7):F861–F865, 2017.
- [14] C. Lamy, A. Lima, V. LeRhun, F. Delime, C. Coutanceau, and J.M. Léger. Recent advances in the development of direct alcohol fuel cells (DAFC). *Journal of Power Sources*, 105(2):283–296, 2002.
- [15] E. Antolini. Formation of carbon-supported PtM alloys for low temperature fuel cells: A review. *Materials Chemistry and Physics*, 78(3):563–573, 2003.
- [16] H. Liu, C. Song, L. Zhang, J. Zhang, H. Wang, and David P. Wilkinson. A review of anode catalysis in the direct methanol fuel cell. *Journal of Power Sources*, 155(2):95–110, 2006.
- [17] Y.V. Tolmachev and O.A. Petrii. Pt–Ru electrocatalysts for fuel cells: developments in the last decade. *Journal of Solid State Electrochemistry*, 21(3):613–639, 2017.
- [18] E. Antolini. Catalysts for direct ethanol fuel cells. *Journal of Power Sources*, 170(1):1–12, 2007.
- [19] J. Friedl and U. Stimming. Model catalyst studies on hydrogen and ethanol oxidation for fuel cells. *Electrochimica Acta*, 101:41–58, 2013.
- [20] S. Beyhan, C. Coutanceau, J.M. Léger, T.W. Napporn, and F. Kadirgan. Promising anode candidates for direct ethanol fuel cell: Carbon supported PtSn-based trimetallic catalysts prepared by Bönemann method. *International Journal of Hydrogen Energy*, 38(16):6830–6841, 2013.

- [21] E. Antolini and E.R. Gonzalez. Alkaline direct alcohol fuel cells. *Journal of Power Sources*, 195(11):3431–3450, 2010.
- [22] S. Sharma and B.G. Pollet. Support materials for PEMFC and DMFC electrocatalysts — A review. *Journal of Power Sources*, 208:96–119, 2012.
- [23] A.L. Dicks. The role of carbon in fuel cells. *Journal of Power Sources*, 156(2):128–141, 2006.
- [24] X. Yu and S. Ye. Recent advances in activity and durability enhancement of Pt/C catalytic cathode in PEMFC. Part I. Physico-chemical and electronic interaction between Pt and carbon support, and activity enhancement of Pt/C catalyst. *Journal of Power Sources*, 172(1):133–144, 2007.
- [25] L. Calvillo, M.J. Lázaro, E. García-Bordejé, R. Moliner, P.L. Cabot, I. Esparbé, E. Pastor, and J.J. Quintana. Platinum supported on functionalized ordered mesoporous carbon as electrocatalyst for direct methanol fuel cells. *Journal of Power Sources*, 169(1):59–64, 2007.
- [26] I. Martin-Gullon, J. Vera, J.A. Conesa, J.L. González, and C. Merino. Differences between carbon nanofibers produced using Fe and Ni catalysts in a floating catalyst reactor. *Carbon*, 44(8):1572–1580, 2006.
- [27] B. Zhang, F. Kang, J.M. Tarascon, and J.K. Kim. Recent advances in electrospun carbon nanofibers and their application in electrochemical energy storage. *Progress in Materials Science*, 76:319–380, 2016.
- [28] Y. Shao, G. Yin, J. Zhang, and Y. Gao. Comparative investigation of the resistance to electrochemical oxidation of carbon black and carbon nanotubes in aqueous sulfuric acid solution. *Electrochimica Acta*, 51(26):5853–5857, 2006.

- [29] S. Guo, S. Dong, and E. Wang. Three-dimensional Pt-on-Pd bimetallic nanodendrites supported on graphene nanosheet: Facile synthesis and used as an advanced nanoelectrocatalyst for methanol oxidation. *ACS Nano*, 4(1):547–555, 2010.
- [30] B.F. Machado and P. Serp. Graphene-based materials for catalysis. *Catal. Sci. Technol.*, 2(1):54–75, 2012.
- [31] Y. Shao, J. Liu, Y. Wang, and Y. Lin. Novel catalyst support materials for PEM fuel cells: current status and future prospects. *J. Mater. Chem.*, 19(1):46–59, 2009.
- [32] E. Antolini and E.R. Gonzalez. Polymer supports for low-temperature fuel cell catalysts. *Applied Catalysis A: General*, 365(1):1–19, 2009.
- [33] G.M. Alvarenga and H.M. Villullas. Transition metal oxides in the electrocatalytic oxidation of methanol and ethanol on noble metal nanoparticles. *Current Opinion in Electrochemistry*, 4(1):39–44, 2017.
- [34] Z. Zhang, J. Liu, J. Gu, L. Su, and L. Cheng. An overview of metal oxide materials as electrocatalysts and supports for polymer electrolyte fuel cells. *Energy Environ. Sci.*, 7(8):2535–2558, 2014.
- [35] N.R. Elezovic, V.R. Radmilovic, and N.V. Krstajic. Platinum nanocatalysts on metal oxide based supports for low temperature fuel cell applications. *RSC Adv.*, 6(8):6788–6801, 2016.
- [36] H. Song, X. Qiu, X. Li, F. Li, W. Zhu, and L. Chen. TiO₂ nanotubes promoting Pt/C catalysts for ethanol electro-oxidation in acidic media. *Journal of Power Sources*, 170(1):50–54, 2007.

- [37] X. He and C. Hu. Building three-dimensional Pt catalysts on TiO₂ nanorod arrays for effective ethanol electrooxidation. *Journal of Power Sources*, 196(6):3119–3123, 2011.
- [38] K. Miecznikowski. Enhancement of activity of PtRh nanoparticles towards oxidation of ethanol through modification with molybdenum oxide or tungsten oxide. *Journal of Solid State Electrochemistry*, 16(8):2723–2731, 2012.
- [39] L. Jiang, G. Sun, Z. Zhou, S. Sun, Q. Wang, S. Yan, H. Li, J. Tian, J. Guo, B. Zhou, and Q. Xin. Size-controllable synthesis of monodispersed SnO₂ nanoparticles and application in electrocatalysts. *The Journal of Physical Chemistry B*, 109(18):8774–8778, 2005.
- [40] A. Kowal, S.L. Gojković, K.S. Lee, P. Olszewski, and Y.E. Sung. Synthesis, characterization and electrocatalytic activity for ethanol oxidation of carbon supported Pt, Pt-Rh, Pt-SnO₂ and Pt-Rh-SnO₂ nanoclusters. *Electrochemistry Communications*, 11(4):724–727, 2009.
- [41] D.A. McKeown, P.L. Hagans, L.P.L. Carette, A.E. Russell, K.E. Swider, and D.R. Rolison. Structure of hydrous ruthenium oxides: Implications for charge storage. *The Journal of Physical Chemistry B*, 103(23):4825–4832, 1999.
- [42] W. Dmowski, T. Egami, K.E. Swider-Lyons, C.T. Love, and D.R. Rolison. Local atomic structure and conduction mechanism of nanocrystalline hydrous RuO₂ from X-ray scattering. *The Journal of Physical Chemistry B*, 106(49):12677–12683, 2002.
- [43] F. Peng, C. Zhou, H. Wang, H. Yu, J. Liang, and J. Yang. The role of RuO₂ in the electrocatalytic oxidation of methanol for direct methanol fuel cell. *Catalysis Communications*, 10(5):533–537, 2009.

- [44] M.L. Calegari, H.B. Suffredini, S.A.S. Machado, and L.A. Avaca. Preparation, characterization and utilization of a new electrocatalyst for ethanol oxidation obtained by the sol-gel method. *Journal of Power Sources*, 156(2):300–305, 2006.
- [45] R.B. Moghaddam and P.G. Pickup. Support effects on the oxidation of ethanol at Pt nanoparticles. *Electrochimica Acta*, 65:210–215, 2012.
- [46] D.D. James, R.B. Moghaddam, B. Chen, and P.G. Pickup. Ruthenium-tin oxide/carbon supported platinum catalysts for electrochemical oxidation of ethanol in direct ethanol fuel cells. *Journal of The Electrochemical Society*, 165(3):F215–F219, 2018.
- [47] L.A. Soares, C. Morais, T.W. Napporn, K.B. Kokoh, and P. Olivi. Beneficial effects of rhodium and tin oxide on carbon supported platinum catalysts for ethanol electrooxidation. *Journal of Power Sources*, 315:47–55, 2016.
- [48] T.M. Brueckner and P.G. Pickup. Kinetics and stoichiometry of methanol and ethanol oxidation in multi-anode proton exchange membrane cells. *Journal of The Electrochemical Society*, 164(12):F1172–F1178, 2017.
- [49] J.M. Lee, S.B. Han, Y.W. Lee, Y.J. Song, J.Y. Kim, and K.W. Park. RuO₂-SnO₂ nanocomposite electrodes for methanol electrooxidation. *Journal of Alloys and Compounds*, 506(1):57–62, 2010.
- [50] M.J. Lázaro, L. Calvillo, V. Celorrio, J.I. Pardo, S. Perathoner, and R. Moliner. Study and application of Vulcan XC-72 in low temperature fuel cells. In *Carbon Black: Production, Properties and Uses*, number January, pages 41–68. 2011.
- [51] Y. Garsany, O.A. Baturina, K.E. Swider-lyons, and S.S. Kocha. Experimental methods for quantifying the activity of platinum electrocatalysts for the oxygen. *Analytical Chemistry*, 82(15):6321–6328, 2010.

- [52] L. An, T.S. Zhao, and Y.S. Li. Carbon-neutral sustainable energy technology: Direct ethanol fuel cells. *Renewable and Sustainable Energy Reviews*, 50:1462–1468, 2015.
- [53] A. Scheithauer, E. von Harbou, H. Hasse, T. Grutzner, C. Rijksen, and D. Zollinger. Droplet microfluidics on a planar surface. *AIChE Journal*, 61(1):177–187, 2015.
- [54] S. Ramachandran and U. Stimming. Well to wheel analysis of low carbon alternatives for road traffic. *Energy and Environmental Science*, 8(11):3313–3324, 2015.
- [55] J.P.I. De Souza, S.L. Queiroz, K. Bergamaski, E.R. Gonzalez, and F.C. Nart. Electro-oxidation of ethanol on Pt, Rh, and PtRh electrodes. A study using DEMS and in-situ FTIR techniques. *Journal of Physical Chemistry B*, 106(38):9825–9830, 2002.
- [56] N. Erini, V. Beermann, M. Gocyla, M. Gliech, M. Heggen, R.E. Dunin-Borkowski, and P. Strasser. The effect of surface site ensembles on the activity and selectivity of ethanol electrooxidation by octahedral PtNiRh nanoparticles. *Angewandte Chemie International Edition*, 56(23):6533–6538, 2017.